Control of energy dissipation between a periodically driven Hubbard model and a fermionic bath

Master Thesis

submitted by

Hristiana Atanasova

Supervisors:

Prof. Dr. Alexander Lichtenstein

Dr. Guy Cohen

University Hamburg

August 2018

Hiermit erkläre ich, dass ich die vorliegende Arbeit selbstständig verfasst und keine anderen als die angegebenen Quellen und Hilfsmittel verwendet habe. Ebenso versichere ich, dass diese Arbeit oder Teile daraus weder von mir selbst noch von anderen als Leistungsnachweis andernorts eingereicht wurden. Die eingereichte schriftliche Fassung entspricht der auf dem elektronischen Speichermedium. Ich bin mit der Veröffentlichung dieser Arbeit einverstanden.

Hamburg, den 03.08.2018   _____

Abstract

The aim of this thesis is to study strongly correlated electronic systems out of equilibrium and to understand how electron-electron interactions affect the energy dissipation between the system and the environment it is coupled to. Tools were developed to investigate the nonequilibrium steady state of a dissipative Hubbard model driven by a periodic electric field. The dissipation is realized by coupling each lattice site to a noninteracting fermionic bath. Despite its simplicity, the Hubbard model has become a paradigmatic model for the study of strongly correlated materials, because it successfully describes the complex electronic behavior that arises from the competition between localization and delocalization effects. The system was studied by means of dynamical mean field theory, a method that maps the many body system onto a single-site impurity problem by treating spatial fluctuations on a mean-field level, while capturing temporal fluctuations accurately. The numerical implementation relies on the lowest order self-consistent hybridization expansion, which provides qualitatively reliable results in the Mott insulating regime.

The focus of our studies lays on the energy current between system and bath, induced by the electric field, as well as the emergence of nonequilibrium distributions and density of states. We show that periodical resonant driving of a Mott insulating system enables a precise control of the dissipation current as well as the system's effective temperature and doublon density by tuning the amplitude of the electric field.

Zusammenfassung

Das Ziel dieser Arbeit ist stark korrelierte elektronische Systeme im Nichtgleichgewicht zu untersuchen und zu verstehen, wie Elektron-Elektron-Wechselwirkungen die Energiedissipation zwischen dem System und seiner Umgebung beeinflussen. Es wurden Mittel entwickelt, um den Nichtgleichgewichtszustand eines dissipativen Hubbard-Modells zu untersuchen, das von einem periodischen elektrischen Feld getrieben wird. Die Dissipation wird durch die Kopplung jeder Gitterstelle an ein nicht wechselwirkendes fermionisches Bad realisiert. Trotz seiner Einfachheit hat das Hubbard-Modell sich zu einem paradigmatischen Modell für die Untersuchung stark korrelierter Materialien etabliert. Es beschreibt das komplexe elektronische Verhalten, das aus der Konkurrenz zwischen Lokalisations- und Delokalisierungseffekten entsteht. Das System wurde mittels der Dynamischen Mittelfeldtheorie untersucht, einer Methode, die das Vielteilchensystem auf ein Einteilchenproblem abbildet. Dabei werden räumliche Fluktuationen auf Molekularfeldebene behandelt, während zeitliche Fluktuationen exakt beschrieben werden. Die numerische Implementierung basiert auf Störungstheorie bis zur ersten Ordnung in der Hybridisierung, die qualitativ zuverlässige Ergebnisse im isolierenden Mott-regime liefert.

Der Fokus dieser Arbeit liegt auf dem Energiestrom zwischen System und Bad, der durch das elektrische Feld induziert wird, sowie den Nichtgleichgewichtsverteilungen und Zustandsdichten. Wir zeigen, dass periodisches Treiben eines Mott-Isolators eine präzise Kontrolle des Dissipationsstromes sowie der effektiven Temperatur und der Doublondichte des Systems ermöglicht.

Contents

1 Introduction

During the last decade the study of strongly correlated systems out of equilibrium has developed to one of most topical research fields, but so far only a small part of it is considered as being discovered and even a smaller one as understood. While already in equilibrium they bring out fascinating phenomena such as metal-to-Mott-insulator transition or transitions to superconducting states [1, 2, 3], the study of excitation and relaxation processes provide an even deeper insight. The interaction between the electrons and the lattice is difficult to resolve and relaxation paths are not intuitive at all, but driving the system out of equilibrium disentangles certain relaxation channels and gives an additional perspective. The experimental study of excitation and relaxation phenomena has made remarkable progress realized by ultra-fast time-resolved spectroscopy, where the system is excited by an intense laser pulse and the relaxation is recorded with succeeding probe-pulses. Furthermore, simple model Hamiltonians can be studied through ultra cold atoms in optical lattices, which enable a precise control and measurement of the systems's parameters and the possibility to study quench dynamics and field driven effects [1, 4]. On the theoretical side, various methods based on the concept of wave function, density matrix or Green's function formulations have been successfully used to describe nonequilibrium phenomena [5, 6, 2].

Fundamental nonequilibrium phenomena include transport processes governed by external driving fields, which are the main subject of this thesis. In cases where the change to the system is small because the applied fields are small, it is possible to describe the transport adequately by employing approximations which neglect the nonequilibrium nature of the system. These approximations are linear response theory, which treats the driving in a perturbative manner and quantum Boltzmann methods, to name a few [7].

Transport processes can contribute to new technologies when the system is in contact with an environment, with which it can exchange energy or charge. Additionally, the system needs to have a stable behavior for a given set of external parameters. This is the case when the energy supplied by an external driving is compensated by dissipative mechanisms, which is referred to as a nonequilibrium steady state. A simple example for for this is a classic periodical driven damped harmonic oscillator where, after a transient behavior, the oscillator enters a steady state.

On one hand the application of time-periodic driving has developed as a tool to control many body systems. For cold atom systems this is achieved my modulating the lattice potential [8, 9], while in condensed matter systems strong resonant THz fields are applied to alter electronic excitations [10]. The ultrafast control of magnetism, which may be useful for magnetic storage devices, is one of the fundamental topics of interest. On the other hand, progress has been made by new experimentally realized nonlinear transport devices

[8]. Motivated by these developments we examine how a strong periodic driving influences the energy transport between a system and its environment considering a repulsive Hubbard model coupled to a noninteracting fermionic bath.

In section 2 we are introducing the iconic Hubbard model, which is studied by means of Dynamical Mean Field Theory. We will explain the ideas and basic principles of Dynamical Mean Field Theory, which require the solution of impurity systems. The last part of this section extends the model to an open system by introducing a dissipation mechanism. Section is dedicated to the specific realization of the dissipative Hubbard model, driven by an electric field, and its numerical implementation as well as the initial setup of the system. The results of this work are presented in section 4 where we start out with testing our numerical implementation and comparing it to research realized by other groups. The second half presents the results for the full setup introduced in section 3. Finally, section 5 gives a summary as well as a discussion of the main results obtained within this thesis, after which we point out open questions and future projects.

2 Theoretical concepts

This chapter starts with the introduction of the Hubbard model, which describes correlated electronic systems and will later be extended to an open model (subsection 2.5). We will further provide a method (subsection 2.2 and 2.3), the dynamical mean field theory, which has over the last decades proven to be successful for the study of strongly correlated systems by treating spatial fluctuations on a mean-field level, while capturing temporal fluctuations accurately. Its major contribution in understanding correlated materials was the successful description of metal-to-Mott-insulator transition. For an extensive review see [11]. The mean-field treatment of spatial fluctuations allows for a self-consistent mapping of the whole system onto a single-site impurity problem. Solving the impurity problem remains a challenging but feasible task, which is addressed in subsection 2.4.

2.1 Hubbard model

During its 50-year history the Hubbard model has, despite its simplicity, become a paradigmatic model for the study of strongly correlated materials. It was introduced by Anderson, Hubbard, Gutzwiller and Kanamori in 1963 for the study of correlated d-electrons in transition metals [12, 13, 14], showing behavior that arises from the competition between localization and delocalization effects. The Hamiltonian describes a collection of single levels associated with Wannier orbitals centered at each site of the crystal lattice and is given by

$$H_{Hubbard} = - \sum_{\langle i,j \rangle, \sigma}^{N} t_{ij} d_{i\sigma}^{\dagger} d_{j\sigma} + \epsilon_0 \sum_{i,\sigma}^{N} d_{i\sigma}^{\dagger} d_{i\sigma} + U \sum_{i}^{N} d_{i\uparrow}^{\dagger} d_{i\uparrow} d_{i\downarrow}^{\dagger} d_{i\downarrow}, \tag{1}$$

where N is the number of lattice sites and the operator $d_{i\sigma}^{\dagger} (d_{i\sigma})$ creates (destroys) an electron with spin σ at the lattice site i with coordinate $\mathbf{R}_i$. The first term on the right hand side describes a single tight-binding band and the term

$$t_{ij} = \frac{1}{N} \sum_{\mathbf{k}} \epsilon_{\mathbf{k}} e^{i\mathbf{k}(\boldsymbol{R}_i - \boldsymbol{R}_j)}$$

is the amplitude for an electron to hop between site i and j. Its magnitude depends on the overlap between the orbitals. Since the hopping amplitude decreases strongly with increasing site distance, we take only nearest neighbor hopping into account. The second term is the on-site energy and the last one the Coulomb repulsion of two electrons with opposite spin occupying the same orbital. Because the bands are assumed to be strongly localized at the lattice sites, electron interactions between different sites are neglected.

The Hubbard Model captures the competition between two key energy scales: the kinetic
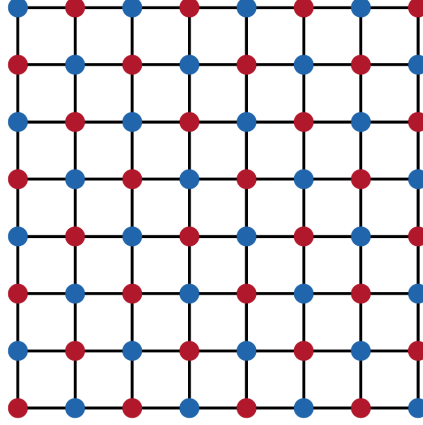
Figure 1: Schematic representation of the Hubbard model with two sublattices.

energy and the Coulomb repulsion. In the absence of hopping the model reduces to the four atomic states $|0\rangle, |\uparrow\rangle, |\downarrow\rangle$ and $|\uparrow\downarrow\rangle$ with energies $0, \epsilon_0, U + 2\epsilon_0$. A system at half filling, corresponding to $\epsilon_0 = -\frac{U}{2}$, simplifies the discussion by guaranteeing particle-hole symmetry. The limiting cases regarding the Coulomb interaction are often considered to gain further insight to the model:

- In the limit of $U \to 0$ the model reduces to a single-band tight-binding model representing a metal

- For $U \to \infty$ the electrons are strongly localized and the system becomes a so-called Mott insulator

The crossover between those limits, when the kinetic energy and the Coulomb repulsion are competing, opens up a variety of new physical phenomena [15, 16, 17] and is essential for the understanding of strongly correlated materials.

2.2 Overview of equilibrium dynamical mean field theory

Dynamical Mean Field Theory (DMFT) is a powerful approximation when it comes to the study of many body systems involving strong electronic correlations in as well as out of equilibrium [18, 2]. We will start with a brief overview of the DMFT equations in equilibrium and extend them to the nonequilibrium analogue in the next chapter. The idea of DMFT is to solve the lattice problem with many degrees of freedom by mapping it to an impurity problem consisting of a single correlated site embedded in an uncorrelated bath, formed by the residual sites of the lattice. The hybridization between the impurity and the bath is the dynamical mean field $\Delta(t, t')$. It resembles the exchange of particles with the rest of the lattice and must be determined self consistently as a functional of the lattice Green's function

$G_{ij}(t, t')$. The Green's functions considered here, are one particle correlation functions of the form $G_{ij}(t, t') = i\langle d_i^\dagger(t')d_j(t)\rangle$ and will be addressed in Ch. (2.4.1). The key approximation is the local nature of the lattice self energy

$$\Sigma_{ij}(t, t') \simeq \delta_{ij}\Sigma_{ii}(t, t'). \tag{2}$$

Since in equilibrium all functions depend only on time-differences, they are represented in frequency space by their Fourier transforms. As mentioned in the last chapter, the simplest model for the description of strongly correlated systems is the single band Hubbard model representing a collection of single orbital atoms placed at the nodes of a crystal lattice. For a system at half-filling the Hamiltonian reads as

$$H_{Hubbard} = -\sum_{\langle i,j\rangle,\sigma} t_{ij}d_{i\sigma}^\dagger d_{j\sigma} + \sum_i U(d_{i\uparrow}^\dagger d_{i\uparrow} - \frac{1}{2})(d_{i\downarrow}^\dagger d_{i\downarrow} - \frac{1}{2}).$$

With the approximation that the lattice self energy is local in space the local Green's function

$$G_{ii}^\sigma(t - t') = -i\langle \mathcal{T} d_{i\sigma}(t)d_{i\sigma}^\dagger(t')\rangle,$$

where $\mathcal{T}$ is the time ordering operator, can be computed from an effective impurity model described by the action

$$S_i = i\int_c dt U n_\uparrow(t)n_\downarrow(t) - i\sum_\sigma \int_c dtdt' d_\sigma^\dagger(t)\Delta_i(t - t')d_\sigma(t'). \tag{3}$$

At time t' an electron hops from the fictitious bath to the dot and goes back to the bath at time t, where $\Delta_i(t - t')$ is the amplitude for this process to happen. Whenever two electrons occupy the same site simultaneously this results in an energy cost U, hence the action captures the fluctuation between the four atomic states $|0\rangle, |\uparrow\rangle, |\downarrow\rangle$ and $|\uparrow\downarrow\rangle$. It is important to see that DMFT is a mean field only in terms of spacial fluctuations, which are frozen, but it takes account of all local temporal fluctuations, hence the name "dynamical". From here on the spin index will be suppressed for simplicity.

To solve the impurity problem means to compute the impurity Greens's functions, which can be challenging, but is still feasible. This is considered in subsection 2.4. Once the impurity Green's function is obtained, the impurity self-energy is extracted from the Dyson equation

$$G_{ii}^{-1}(\omega) = \omega + \mu - \Delta_i(\omega) - \Sigma_{ii}^{imp}(\omega),$$

where $\mathcal{G}_0^{-1}(\omega) = \omega + \mu - \Delta_i(\omega)$ is the noninteracting Green's function, known as the "Weiss

function". The approximation for the self-energy (2) is then used to obtain the lattice Green's function

$$G_{ij}^{-1}(\omega) = \delta_{ij}[\omega + \mu - \Sigma_{ii}^{imp}(\omega)] - v_{ij}.$$

In real space this means that all nonlocal components of the lattice self-energy $\Sigma_{ij}(\omega)$ are neglected and the local component corresponds to $\Sigma_{ii}^{imp}(\omega)$. For a translationally invariant system ($\Sigma_{ii}(\omega) \equiv \Sigma(\omega)$) one averages over the whole Brillouin zone to get the on-site component of the lattice Green's function, which is referred to as the self-consistency condition

$$G_{ii}(\omega) = \frac{1}{N} \sum_{\boldsymbol{k}} G_{\boldsymbol{k}}(\omega) = \frac{1}{N} \sum_{\boldsymbol{k}} \frac{1}{\omega + \mu + \Sigma(\omega) - \epsilon_{\boldsymbol{k}}},$$

with $G_{\boldsymbol{k}}(\omega)$ the momentum resolved Green's function, N the number of lattice sites and $\epsilon_{\boldsymbol{k}}$ the dispersion relation of the noninteracting tight binding band

$$\epsilon_{\boldsymbol{k}} = \sum_{j} t_{ij} e^{i\boldsymbol{k}(\boldsymbol{R}_i - \boldsymbol{R}_j)}.$$

Instead of performing the k-summation one can integrate over the local, noninteracting density of states $D(\epsilon) = \frac{1}{N} \sum_{\boldsymbol{k}} \delta(\epsilon - \epsilon_{\boldsymbol{k}})$:

$$G_{ii}(\omega) = \int d\epsilon \frac{D(\epsilon)}{\omega + \mu + \Sigma(\omega) - \epsilon}.$$

The self-consistency condition relates for each frequency ω the dynamical mean field to the local lattice Green's function. This functional relation G[Δ] provides a closed set of equations to determine $\Delta(\omega)$ and G(ω). This can be done by an iterative procedure that does not depend on the initial guess for $\Delta(\omega)$. In a DMFT cycle the lattice model is mapped onto an auxiliary Anderson impurity model (AIM), which is described in subsection 2.4. A schematic representation of the mapping is shown in Fig. 2. The methods for solving the auxiliary problem are called impurity solvers, a real-time impurity solver based on the strong-coupling expansion is used in this thesis. With the impurity solver the Green's function and a the self-energy are calculated, which are used to update the hybridization function. The hybridization function is then used to start a new DMFT-cycle. This procedure repeats until a convergence criterium is reached.

Metzner and Vollhart [19] showed that in the limit of infinite nearest neighbors, known as the coordination number Z, DMFT becomes exact if the hopping is rescaled according to

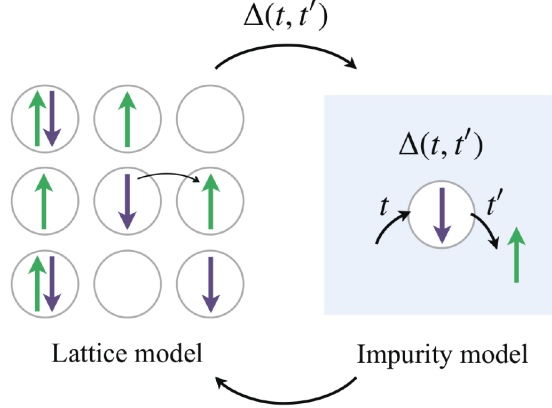$$t_{ij} = \frac{v_{ij}}{\sqrt{Z}},$$

Figure 2: Schematic representation of the DMFT formalism, where the lattice model is mapped onto an impurity problem. $\Delta(t, t')$ is the hybridization between the single site and the bath [18].

with a constant v_{ij} ensuring that the kinetic energy remains finite and the competition between kinetic and potential energy is preserved. The approximation for the self-energy (2) then holds exactly

$$\lim_{Z \to \infty} \Sigma_{ij}(t, t') = \delta_{ij} \Sigma_{ii}(t, t').$$

Several proofs for this exist including a linked cluster expansion around the atomic limit [20] or a cavity method approach [2]. It is quite intuitive that if the number of nearest neighbors is very large, spatial fluctuations become negligible. Other exact solutions are given in the noninteracting limit ($U = 0$), where the local lattice Green's function reduces to $G_{ii}(\omega) = \mathcal{G}_0^{-1}(\omega)$, and in the atomic limit ($t_{ij} = 0$), where the system is a collection of disconnected sites.

2.3 Nonequilibrium DMFT formalism

To capture nonequilibrium physics in time-dependent systems (e.g. an electric-field driven lattice system) all objects within the set of DMFT equations need to incorporate the overall temporal evolution of the system as well as quantum fluctuations. Analogous to the equilibrium case, in the limit $Z \to \infty$ the self energy is local in space:

$$\Sigma_{ij}(t, t') = \delta_{ij} \Sigma_i(t, t').$$

It is used to obtain the contour-ordered lattice Green's function $G_{ij}(t, t') = -i\langle \mathcal{T} d_i(t) d_j^\dagger(t') \rangle$ from the Dyson equation

$$G_{ij}^{-1}(t, t') = (G_0^{-1})_{ij}(t, t') - \delta_{ij} \Sigma_{ii}(t, t'),$$

with the noninteracting lattice Green's function $(G_0^{-1})_{ij}(t,t')$. As for an equilibrium system the effective impurity action

$$S_i = i\int_c dt U n_\uparrow(t) n_\downarrow(t) - i\sum_\sigma \int_c dt dt' d_\sigma^\dagger(t)\Delta_i(t,t')d_\sigma(t')$$

needs to be solved as part of an iterative procedure until the impurity Green's function corresponds to the local lattice Green's function. The equations for nonequilibrium DMFT look formally identical to the ones presented in the previous chapter, but depend on two times and have a nonmarkovian structure.

2.4 Solving the Anderson impurity model

It was first shown by Georges and Kotliar in 1992 [21] that the Hubbard model in infinite Z is equivalent to the Anderson impurity model (AIM)

$$H_{imp} = H_D + H_B + H_{hyb}, \tag{4}$$

with the dot Hamiltonian

$$H_D = \sum_{\sigma\epsilon\uparrow,\downarrow} \varepsilon_\sigma d_\sigma^\dagger d_\sigma + U d_\uparrow^\dagger d_\uparrow d_\downarrow^\dagger d_\downarrow.$$

Here, ε_σ are the on-site energy levels and U is the interaction between electrons having opposite spins. H_{imp} can in general incorporate a time-dependence, but for now we will consider only time-independent impurity models. There are four possible dot eigenstates $|0\rangle, |\uparrow\rangle, |\downarrow\rangle, |\uparrow\downarrow\rangle$ corresponding to the dot being empty or occupied by either one or two electrons. The noninteracting bath Hamiltonian has the form

$$H_B = \sum_{\sigma,k} \varepsilon_k b_k^\dagger b_k,$$

and the coupling between dot and bath is given by the hybridization

$$H_{hyb} = \sum_{\sigma,k} (v_{\sigma k} b_k^\dagger d_\sigma + v_{\sigma k}^* d_\sigma^\dagger b_k),$$

which describes processes in which electrons hop from the bath to the dot and vice versa. The AIM (4) is the hamiltonian representation of the action (3), which can be seen by integrating out the quadratic bath contribution $b_k^\dagger b_k$. This auxiliary model is solved self-consistently as part of the DMFT cycle.

2.4.1 Physical observables and the contour idea

Expectation values of observables $\langle O(t) \rangle$, where $\langle \cdots \rangle$ denotes a quantum and a statistical average, can be related to experimental measurements. If the measurement is time dependent, a framework which tracks the temporal evolution of the statistical ensemble is desirable. Our main goal is to calculate the time dependent correlation of these observables, such as

$$\langle O(t)O(t') \rangle.$$

Knowing all correlations of all observables, would fully describe the system. In second quantization these correlations come in pairs of creation and annihilation operators, which are called Green's functions. A n-particle Green's function with the creation and annihilation operators $d^{(\dagger)}(t_i)$ is given by

$$G_n(t_1, ..., t_n; t'_n, ..., t'_1) = (-i)^n \langle d(t_1)...d(t_n)d^\dagger(t'_n)...d^\dagger(t'_1) \rangle.$$

The operators obey the commutation (anti-commutation) relations for bosons (fermions)

$$[d(t_i), d(t_j)]_{-(+)} = \left[d^\dagger(t_i), d^\dagger(t_j)\right]_{-(+)} = 0,$$

$$\left[d(t_i), d^\dagger(t_j)\right]_{-(+)} = \delta(t_i, t_j).$$

We are interested in the calculation of one-particle correlation functions like $G^>(t, t') = -i\langle d(t)d^\dagger(t') \rangle$ and $G^<(t, t') = i\langle d^\dagger(t')d(t) \rangle$ from which information about physical properties of the system, like the density of single particle excitations, can be extracted.

The expectation value $\langle \cdots \rangle$ of an operator O at time t is given by

$$\langle O(t) \rangle = tr\left(\rho U^\dagger(t_0, t)\hat{O}U(t, t_0)\right),$$

with the time evolution operator $U(t, t_0)$, which propagates a quantum system in time. The initial density matrix ρ is assumed to factorize into the dot ρ_D and the bath ρ_B density matrix, since the dot is initially decoupled from the bath. If one reads the trace from left to the right, it could be interpreted as the oriented contour depicted in Fig. 3: States are propagated from time t_0 to t, then an operator acts at time t, after which the states are propagated back to t_0. The forward (backward) propagation is represented by $U(t, t_0)$ $(U^\dagger(t, t_0))$, which exists on the upper (lower) contour branch. It is assumed that the system starts out in a mixed state in thermal equilibrium under $H^M(t_0) = H(t_0) - \mu N(t_0)$, with the time t_0 at which the system starts propagating in time, the chemical potential μ and the particle number operator N. The mixed state with the inverse temperature β can be represented by the density operator
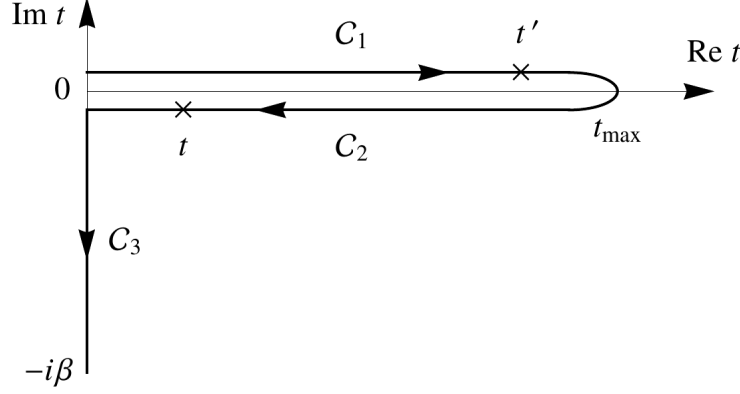
Figure 3: The L-shaped contour in the Kadanoff-Baym formalism describes an oriented curve in the complex plane. The arrows indicate the orientation $t > t'$ along the curve [18].

$$\rho = \frac{e^{-\beta H^M(t_0)}}{Z},$$

where $Z = tr\left(e^{-\beta H^M(t_0)}\right)$ is the thermal equilibrium partition function. Then the exponential can be viewed as a propagation in imaginary time up to $-i\beta$ along the Matsubara contour[22].

Usually an expectation value $\langle \cdots \rangle$ is obtained by splitting H_{imp} into a sum $H_{imp} = H_0 + H_{int}$, the time propagation is computed exactly in H_0 and H_{int} is treated by a formal perturbative expansion. For a weak electronic coupling, known as the weak-coupling approach, the expansion is performed in terms of the parameter U. In the strong-coupling approach, the one used in this thesis, a large U is assumed and H_D and H_B sum up to H_0, while the expansion is performed in terms of H_{hyb}, which is demonstrated in the following.

In the interaction picture the operators, here denoted by a hat, have the time dependence

$$\hat{O}(t) = e^{iH_0 t} O e^{-iH_0 t},$$

with the reduced Hamiltonian $H_0 = H_{imp} - H_{hyb}$ containing information about the electron coupling U. The interaction picture time evolution propagator is given by

$$U(t) = e^{iH_0 t} e^{-iHt}$$

and obeys the the differential equation

$$\frac{\partial}{\partial t}U(t) = ie^{iH_0 t}(H_0 - H)e^{-iH_0 t}$$
$$= -ie^{iH_0 t}H_{hyb}(e^{-iH_0 t}e^{iH_0 t})e^{iHt}$$
$$= -i\widehat{H}_{hyb}(t)U(t).$$

After integrating both sides with respect to time

$$U(t) = 1 - i\int_0^t dt_1 \widehat{H}_{hyb}(t_1)U(t_1)$$

and after repeatedly iterating we arrive at

$$U(t) = \sum_{n=0}^{\infty}(-i)^n \int_0^t dt_1 \int_0^{t_1} dt_2 \cdots \int_0^{t_{n-1}} dt_n \widehat{H}_{hyb}(t_1)\widehat{H}_{hyb}(t_2)\cdots\widehat{H}_{hyb}(t_n) \tag{5}$$

with time ordering $t_1 > t_2 > \ldots > t_n$. The Hybridization term in the interaction picture can be written in the following form:

$$\widehat{H}_{hyb}(t) = e^{iH_0 t}V e^{-iH_0 t}$$
$$= \sum_{n=0}^{\infty}\frac{i}{n!}^n (H_0 t)^n \sum_{\sigma,k}(v_{\sigma k}b_k^{\dagger}d_{\sigma} + v_{\sigma k}^{\star}d_{\sigma}^{\dagger}b_k)\sum_{n=0}^{\infty}\frac{(-i)}{n!}^n (H_0 t)^n$$
$$= \sum_{\sigma,k}\sum_{n=0}^{\infty}\frac{i}{n!}^n (\varepsilon_{\sigma}d_{\sigma}^{\dagger}d_{\sigma} + Un_{\uparrow}n_{\downarrow} + \varepsilon_k b_k^{\dagger}b_k)^n (t)^n \times$$
$$\sum_{\sigma,k}(v_{\sigma k}b_k^{\dagger}d_{\sigma} + v_{\sigma k}^{\star}d_{\sigma}^{\dagger}b_k)\sum_{n=0}^{\infty}\frac{(-i)}{n!}^n (\varepsilon_{\sigma}d_{\sigma}^{\dagger}d_{\sigma} + Un_{\uparrow}n_{\downarrow} + \varepsilon_k b_k^{\dagger}b_k)^n (t)^n$$

Using $[d_{\sigma}, n_{\uparrow}n_{\downarrow}] = d_{\bar{\sigma}}$ and the Baker–Hausdorff theorem

$$d_{\sigma}(t) = e^{iH_0 t}d_{\sigma}e^{-iH_0 t} = e^{-itL_{H_0}}d_{\sigma},$$

where $L_{H_0}d_{\sigma} \equiv [d_{\sigma}, H_0] = \sum_{\sigma \in \uparrow,\downarrow} \varepsilon_{\sigma}\left[d_{\sigma}, d_{\sigma}^{\dagger}d_{\sigma}\right] = \sum_{\sigma \in \uparrow,\downarrow} \varepsilon_{\sigma}d_{\sigma}$, we arrive at

$$\widehat{H}_{hyb}(t) = \sum_{\sigma,k}\left\{v_{\sigma k}e^{i(\varepsilon_{\sigma} + Ud_{\bar{\sigma}}^{\dagger}d_{\bar{\sigma}} - \varepsilon_{\sigma k})t}b_{\sigma k}^{\dagger}d_{\sigma} + v_{\sigma k}^{\star}e^{-i(\varepsilon_{\sigma} + Ud_{\bar{\sigma}}^{\dagger}d_{\bar{\sigma}} - \varepsilon_{\sigma k})t}d_{\sigma}^{\dagger}b_{\sigma k}\right\}.$$

2.4.2 Green's function computation within the noncrossing approximation

This section follows the work of Cohen et al in [23], which explains how Green's functions are calculated in two steps: first propagators $G_{\alpha\beta}(t)$ between the four many body states are obtained, which do not have any physical meaning, but which are used to calculate probability functions for a dot starting in $|\alpha\rangle$ at time t to be in the state $|\beta\rangle$ at time t'. These probability functions are called Vertex functions $K_{\alpha\beta}(t, t')$. Both, $G_{\alpha\beta}(t)$ and $K_{\alpha\beta}(t, t')$ are then used to construct the correlation functions $G_{\alpha\sigma}^{>/<}(t, t')$.

Instead of summing over all diagrams generated by the hybridization expansion, we only take into account diagrams without crossing hybridization lines, which correspond to the lowest order in perturbation theory. This method is known as the noncrossing approximation (NCA) and has been commonly used as an impurity solver for DMFT for many years [24, 25]. The reason for this are its conserving nature and good convergence properties in the Mott insulating regime [4]. Its drawbacks are that it gives reliable results down to the Kondo temperature T_K, but fails in the Fermi-liquid regime for $T \ll T_K$ [26].

Bold propagators

A bold propagator $G_{\alpha\beta}(t)$ between the many body states α and β contains all hybridization lines in a given time interval within the NCA, that exist only on one branch. Propagators on the upper and lower branch obey the relation $G_{\alpha\beta}^\dagger(t) = G_{\alpha\beta}(\bar{t})$. Starting from the formal expression

$$G_{\alpha\beta}(t) = \langle\langle \alpha \mid \rho_D e^{-iHt} \mid \beta\rangle\rangle_B = \langle\langle \alpha \mid \rho_D e^{-iH_0 t} U(t) \mid \beta\rangle\rangle_B,$$

where $\langle \cdots \rangle_B = Tr\{\rho_B \cdots\}$ denotes that the bath degrees are traced out, the expansion for the time evolution operator $U(t)$ of Eq. 5 can be inserted:

$$G_{\alpha\alpha}(t) = \langle\langle \alpha \mid \rho_D e^{-iH_0 t} \mid \alpha\rangle\rangle_B + (-i)^2 \int_0^t dt_1 \int_0^{t_1} dt_2 \langle\langle \alpha \mid \rho_D e^{-iH_0 t} \widehat{H}_{hyb}(t_1)\widehat{H}_{hyb}(t_2) \mid \alpha\rangle\rangle_B + \cdots$$

$$= \sum_\beta \langle\langle \alpha \mid \beta\rangle\langle\beta \mid e^{-iH_0 t} \mid \alpha\rangle\rangle_B - \sum_\beta \sum_{\sigma,\lambda} \int dt_1 \int_0^{t_1} dt_2 \, |t_{\sigma\lambda}|^2 \times$$

$$(\langle\langle \alpha \mid e^{-iH_0 t} d_\sigma \mid \beta\rangle\langle\beta \mid d_\sigma^\dagger \hat{b}_{\sigma\lambda}^\dagger(t_1)\hat{b}_{\sigma\lambda}(t_2) \mid \alpha\rangle\rangle_B$$

$$+ \langle\langle \alpha \mid e^{-iH_0 t} d_\sigma^\dagger \mid \beta\rangle\langle\beta \mid d_\sigma \hat{b}_{\sigma\lambda}(t_2)\hat{b}_{\sigma\lambda}^\dagger(t_1) \mid \alpha\rangle\rangle_B) + \dots$$

$$= \delta_{\alpha\beta}e^{-i\varepsilon_\alpha t} - \sum_\beta \int_0^t dt_1 \int_0^{t_1} dt_2 G_{\alpha\alpha}^{(0)}(t-t_1)G_{\beta\beta}^{(0)}(t_1-t_2) \times$$

$$(\langle \alpha \mid d_\sigma \mid \beta \rangle\langle \beta \mid d_\sigma^\dagger \mid \alpha \rangle \sum_{\sigma,\lambda} |t_{\sigma\lambda}|^2 \langle \hat{b}_{\sigma\lambda}^\dagger(t_1)\hat{b}_{\sigma\lambda}(t_2)\rangle_B +$$

$$\langle \alpha \mid d_\sigma^\dagger \mid \beta \rangle\langle \beta \mid d_\sigma \mid \alpha \rangle \sum_{\sigma,\lambda} |t_{\sigma\lambda}|^2 \langle \hat{b}_{\sigma\lambda}(t_2)\hat{b}_{\sigma\lambda}^\dagger(t_1)\rangle_B)G_{\alpha\alpha}(t_2) + \cdots$$

$$= G_{\alpha\alpha}^{(0)}(t) - \sum_\beta \int_0^t dt_1 \int_0^{t_1} dt_2 G_{\alpha\alpha}^{(0)}(t-t_1)G_{\beta\beta}^{(0)}(t_1-t_2) \times$$

$$(\langle \alpha \mid d_\sigma \mid \beta \rangle\langle \beta \mid d_\sigma^\dagger \mid \alpha \rangle \triangle_\sigma^< (t_1-t_2) + \langle \alpha \mid d_\sigma^\dagger \mid \beta \rangle\langle \beta \mid d_\sigma \mid \alpha \rangle \triangle_\sigma^> (t_1-t_2)) G_{\alpha\alpha}^{(0)}(t_2) + \cdots$$

with the bare atomic state propagators $G_{\alpha\alpha}^{(0)}(t) = \exp^{-i\varepsilon_\alpha t}$ leaving the dot state invariant. Both the bare $G_{\alpha\alpha}^{(0)}(t)$ and bold propagator $G_{\alpha\alpha}(t)$ are diagonal for the Anderson impurity model because the trace over the bath differs from zero only for an even number of creation and annihilation operators, therefore only square terms of $\widehat{H}_{hyb}$ appear in the expansion for the propagators. In DMFT the hybridization function $\Delta_\sigma^{>/<}$ is obtained from the self-consistency condition, but for the initial guess it can be expressed in terms of the coupling density $\Gamma(\omega) = \pi \sum_k |t_k|^2 \delta(\omega - \varepsilon_k)$ that fully describes the bath properties and the hybridization with the initial Fermi Dirac distribution $f(\omega - \mu) = \frac{1}{1+\exp^{\beta(\omega-\mu)}}$

$$\Delta^<(t_1,t_2) = \int_{-\infty}^\infty \frac{d\omega}{\pi} e^{-i\omega(t_1-t_2)} \Gamma(\omega)f(\omega - \mu) \tag{6}$$

and

$$\Delta^>(t_1,t_2) = \int_{-\infty}^\infty \frac{d\omega}{\pi} e^{-i\omega(t_1-t_2)} \Gamma(\omega)(1 - f(\omega - \mu)).$$

With the approximation for the self-energy, that it includes only noncrossing hybridization lines, the Dyson equation can be written as

$$G_{\alpha\alpha}(t) = G_{\alpha\alpha}^{(0)}(t) - \int_0^t dt_1 \int_0^{t_1} dt_2 G_{\alpha\alpha}^{(0)}(t-t_1)\Sigma_{\alpha\alpha}(t_1-t_2)G_{\alpha\alpha}(t_2)$$

with

$$\Sigma_{\alpha\alpha}(t_1-t_2) = \sum_\sigma \sum_\beta G_{\beta\beta}(t_1-t_2) \times$$

$$(\langle \alpha \mid d_\sigma \mid \beta \rangle\langle \beta \mid d_\sigma^\dagger \mid \alpha \rangle\Delta_\sigma^<(t_1-t_2) + \langle \alpha \mid d_\sigma^\dagger \mid \beta \rangle\langle \beta \mid d_\sigma \mid \alpha \rangle\Delta_\sigma^>(t_1-t_2)).$$

A diagrammatic representation of the Dyson equation and the self energies is given in Fig.

13

$$\Sigma_{00} = \text{[diagram]} + \text{[diagram]}$$

$$\Sigma_{11} = \text{[diagram]} + \text{[diagram]}$$

$$\text{[diagram]} = \text{[diagram]} + \text{[diagram]} + \text{[diagram]}$$
$$+ \text{[diagram]} + ...$$

$$\Sigma_{22} = \text{[diagram]} + \text{[diagram]}$$

$$\Sigma_{33} = \text{[diagram]} + \text{[diagram]}$$

Figure 4: Left: Diagrammatic representation of the Dyson equation showing examples of low order diagrams. Right: Diagrams representing the self energy matrix elements within the noncrossing approximation [23].

4. Here upper (lower) lines represent spin up (spin down), dashed lines are empty orbitals and solid lines occupied orbitals and wiggly lines represent an electron which is ejected from or injected to the bath.

For the four different initial states on the dot, denoted by the outer index α, a set of coupled Dyson equations is derived, which can be solved by a self consistent iteration. In equilibrium all entities depend only on time differences and one can evaluate the integrals in the Fourier space by applying the convolution theorem. Before starting with the first iteration, the bold propagators $G_{\alpha\alpha}(t)$ are initialized by the bare propagators $G_{\alpha\alpha}^{(0)}(t)$ from which the first self-energy is obtained. Both are inserted into the Dyson equation with the interaction times integrated over. With the updated $G_{\alpha\alpha}(t)$ one can go back to the second step and compute a new self energy for the next iteration cycle until convergence is reached. Solving the above equations for nonequilibrium system is discussed in subsection 3.6.

Correlation functions

So far we have calculated propagators between many body states, which contain all non-crossing hybridization lines in a time segment on a single branch. These objects have no physical meaning and in order to compute physical observables it is necessary to include hybridization lines connecting times on both branches. We introduce so called vertex functions $K_{\alpha\beta}(t, t')$ with the first (second) time index on the upper (lower) branch. A vertex function incorporates all noncrossing intra- and inter-branch hybridization lines. The procedure to estimate $K_{\alpha\beta}(t, t')$ is similar to the calculation of $G_{\alpha\alpha}(t)$ with the difference that $K_{\alpha\beta}(t, t')$ is a two-times function and instead of four we have 16 equations representing the evolution of the dot from any initial state α to any final state β. For every initial state there are four

coupled equations of the form

$$K_{\alpha\beta}(t,t') = K_{\alpha\beta}^{(0)}(t,t') + \sum_{\gamma\delta} \int_0^t dt_1 \int_0^{t'} dt_2 K_{\alpha\gamma}(t_1,t_2)\Delta_{\gamma\delta}(t_1,t_2)G_{\delta\beta}^\dagger(t-t_1)G_{\delta\beta}(t'-t_2).$$

The vertex functions without inter-branch hybridization lines are composed by the bold propagators on the upper and lower branch

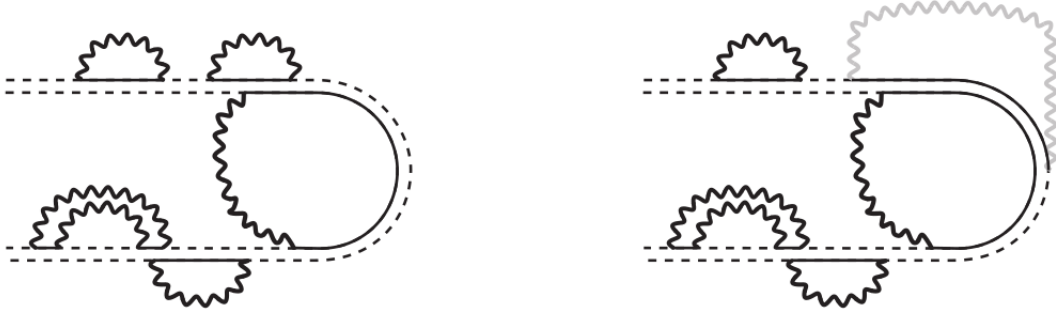$$K_{\alpha\beta}^{(0)}(t,t') = \delta_{\alpha\beta}G_{\alpha\beta}^\dagger(t)G_{\alpha\beta}(t').$$

Figure 5: Left: Example of a diagram contained in the Vertex function $K_{0\downarrow}(t,t')$ with branch crossing hybridization lines. Right: Diagram with a special hybridization line contributing to the correlation function $G_\uparrow^>(t,t')$ [23].

The left diagram in Fig. 5 shows a Vertex function, which contributes to the probability that an initially empty orbital at time t' will be in a spin down state at t. For equal times, $K_{\alpha\beta}(t,t)$ is the population probability on the dot. The right diagram in Fig. 5 has a special hybridization line with a value of 1, which contributes to the correlation function $G_\uparrow^>(t,t')$. After initializing the vertex functions $K_{\alpha\beta}(t,t')$ with $K_{\alpha\beta}^{(0)}(t,t')$ and performing the self-consistent iteration scheme one is able to construct Green's functions in the following way:

$$G_{\alpha\uparrow}^>(t,t') = -i\langle d_\uparrow(t)d_\uparrow^\dagger(t')\rangle = K_{\alpha0}(t,t') * G_\uparrow(t-t') + K_{\alpha\downarrow}(t,t') * G_{\uparrow\downarrow}(t-t')$$

$$G_{\alpha\uparrow}^<(t,t') = i\langle d_\uparrow^\dagger(t')d_\uparrow(t)\rangle = K_{\alpha\uparrow}(t,t') * G_0(t-t') + K_{\alpha\uparrow\downarrow}(t,t') * G_\downarrow(t-t')$$

$$G_{\alpha\downarrow}^>(t,t') = -i\langle d_\downarrow(t)d_\downarrow^\dagger(t')\rangle = K_{\alpha0}(t,t') * G_\downarrow(t-t') + K_{\alpha\uparrow}(t,t') * G_{\uparrow\downarrow}(t-t')$$

$$G_{\alpha\downarrow}^<(t,t') = i\langle d_\downarrow^\dagger(t')d_\downarrow(t)\rangle = K_{\alpha\downarrow}(t,t') * G_0(t-t') + K_{\alpha\uparrow\downarrow}(t,t') * G_\uparrow(t-t')$$

with α denoting the initial dot state.

Properties of the Green's functions

The retarded and advanced component of the Green's function are linked via

$$G^R(t,t') = \left[G^A(t',t)\right]^*$$

and can be defined via the lesser and greater component as

$$\begin{aligned}
G^R(t,t') &= -i\Theta(t-t')\langle\left[d(t),d^\dagger(t')\right]_+\rangle \\
&= -i\Theta(t-t')\left(\langle d(t)d^\dagger(t')\rangle + \langle d^\dagger(t')d(t)\rangle\right) \\
&= \Theta(t-t')\left(G^>(t,t') - G^<(t,t')\right)
\end{aligned}$$

and

$$\begin{aligned}
G^A(t,t') &= i\Theta(t'-t)\langle\left[d(t),d^\dagger(t')\right]_+\rangle \\
&= i\Theta(t'-t)\left(\langle d(t)d^\dagger(t')\rangle + \langle d^\dagger(t')d(t)\rangle\right) \\
&= -\Theta(t'-t)\left(G^>(t,t') - G^<(t,t')\right).
\end{aligned}$$

The lesser and greater component fulfill

$$-G^{>/<}(t,t') = \left[G^{>/<}(t,t')\right]$$

and for particle-hole symmetric system they hold

$$G^{>/<}(t,t') = -G^{>/<}(t',t).$$

The imaginary part of their Fourier transforms gives an intuitive interpretation in terms of the spectral function $A(\omega)$, which corresponds to the density of states.

$$A(\omega) = -\frac{1}{\pi}Im G(\omega)^R = \frac{1}{\pi}Im G(\omega)^A.$$

Out of equilibrium one can still define a spectral function via a partial Fourier transform

$$A(\omega,t) = -\frac{1}{\pi}Im \int_0^t ds e^{i\omega s} G^R(t,t-s), \tag{7}$$

16

which satisfies

$$\int d\omega A(\omega) = 1. \tag{8}$$

The lesser (greater) Green's function contains information about the distribution of occupied (unoccupied) states

$$\mp ImG^<(\omega) = 2\pi A(\omega)F(\omega) \tag{9}$$

$$-ImG^>(\omega) = 2\pi A(\omega)[1 \pm F(\omega)]. \tag{10}$$

The upper signs are valid for bosons and the lower for fermions. Here, $F(\omega)$ represents the nonequilibrium distribution function, in equilibrium coincides with the Bose or Fermi distribution

$$f(\omega) = \frac{1}{(e^{\beta\omega} \mp 1)}.$$

Eqs. (9) and (10) are a generalization of the fluctuation-dissipation theorem to steady states with arbitrary distribution functions [27, 28].

2.5 Dissipative systems

Considering an open system enables the energy injected through the continuous driving field to dissipate into a heat bath, so that a steady state can emerge. An additional purpose is that the exchange of energy and particles with the environment should be included for a realistic description of the system. One can describe dissipation of energy to other degrees of freedom by coupling every site of the lattice to an environment, that has a large number of degrees of freedom, such that it is not influenced by the system and such that system and bath are in thermal equilibrium with temperature T. In DMFT two dissipation mechanisms have been adopted so far. The first one couples each lattice site to a reservoir of noninteracting fermions and thus it is called the free-fermion bath, with the same structure as the bath in the AIM

$$H_f = H_{fBath} + H_{fmix}, \tag{11}$$

with

$$H_{fBath} = \sum_{k,\sigma} \varepsilon_k f^\dagger_{k,\sigma} f_{k,\sigma}$$

and

$$H_{fmix} = \sum_{k,\sigma} (V_k f_{k,\sigma}^\dagger d_\sigma + V_k^* d_\sigma^\dagger f_{k,\sigma}),$$

where $d_\sigma^\dagger (d_\sigma)$ creates (annihilates) an electron on the dot, $f_k^\dagger (f_k)$ creates (annihilates) a bath degree of freedom, ε_k describes the bath energy levels and V_k is the hybridization between the bath modes and the impurity. The bath is in thermal equilibrium with a defined temperature T and a chemical potential μ_k, which is chosen such that there is no current flow between the bath and the impurity.
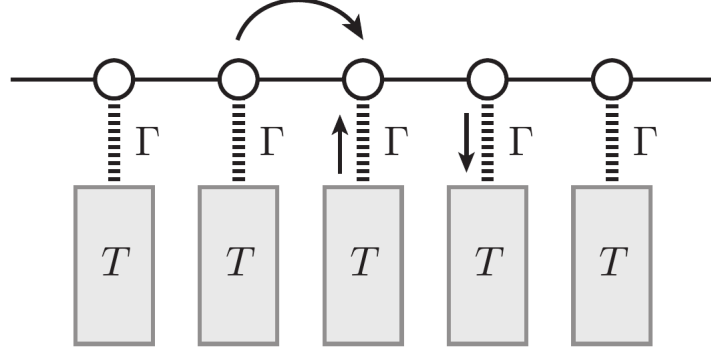

Figure 6: Schematic representation of a noninteracting fermionic bath at temperature T attached to every site of the lattice with the coupling Γ [18].

The second dissipation mechanism is the coupling to a bosonic bath, which can be described via the Holstein coupling with the local phonon bath Hamiltonian

$$H_{phBath} = \sum_q \omega_q b_q^\dagger b_q.$$

Here $b_q^\dagger (b_q)$ are creation (annihilation) operators and ω_q is the frequency of the phonon mode q. The electron-phonon coupling is given by

$$H_{phMix} = \sum_q \lambda_q (b_q^\dagger + b_q)(n_d - 1),$$

where n_d is the total dot occupation and λ_d the coupling strength between the dot and the phonon modes. The term -1 has no physical meaning, but is there to sustain particle-hole symmetry for the energy level $\epsilon = 0$.

The external bath functions not only as a dissipation mechanism so that a steady state can emerge, it also fixes the temperature of the system.

3 Implementation

So far we have introduced the methods and the model only in a general way without an explicit lattice structure. The chosen model in this work is a Bethe lattice depicted in Fig. 7, which is studied by means of the DMFT scheme described in subsection 2.2 and 2.3. The focus lies on the influence of an electric field on the energy current between the system and heat bath it is attached to, the spectral properties and the nonequilibrium distribution function. Analyzing the current as a function of the electric field requires the self-consistent solution of the system's Green's functions for every given value of the electric field, therefore the setup aims to reduce the computational cost.
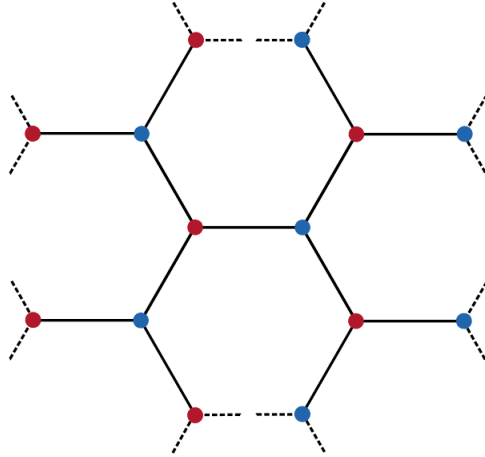
3.1 Bethe lattice and initial setup

Figure 7: Segment of the Bethe lattice with coordination number $Z = 3$ and two sublattices with opposite magnetization. Each site is connected to any other by only one single path.

All results within the scope of this work are performed for a Bethe lattice or Cayley tree, which is an infinite connected cycle-free graph in terms of graph theory. Cycle-free means that there is only one path connecting two sites and each site has Z nearest neighbors. In the DMFT approach it is used in the limit of $Z \rightarrow \infty$, where the self-consistency condition collapses to a simple form

$$\Delta(t, t') = v_0{}^2 G(t, t'), \tag{12}$$

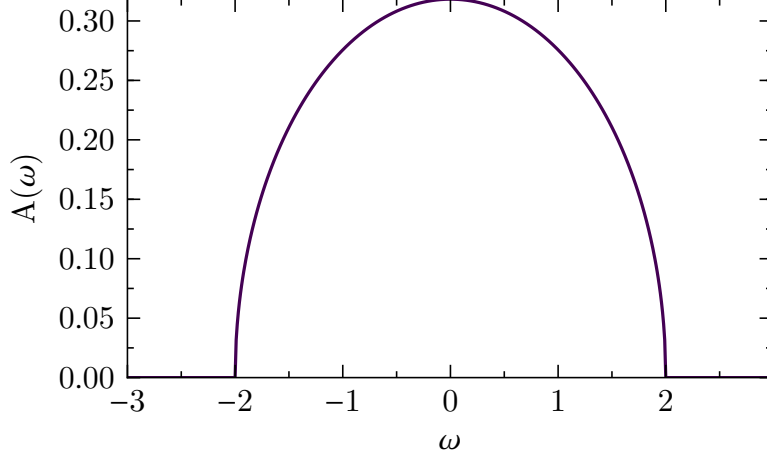which reduces computational cost. A noninteracting Bethe lattice in this limit has a semielliptical DOS

Figure 8: DOS of the non interacting Bethe lattice as described in Eq. 13

$$D(\omega) = \frac{1}{2\pi v_0^2}\sqrt{4v_0^2 - \omega^2}, \omega < 2v_0, \qquad (13)$$

with the band edges at $\omega = \pm 2v_0$, as shown in Fig. 13. If the hopping is such that the bandwidth depends on time, (12) generalizes to [29]

$$\Delta(t,t') = v(t)G(t,t')v^*(t').$$

The systems is set up in the initial Néel state, which is a classical antiferromagnetic state

$$| \psi_{Neel} > = \prod_{i\epsilon A} d_{i\uparrow}^\dagger \prod_{j\epsilon B} d_{j\downarrow}^\dagger | 0 > .$$

It consists of two homogeneous sublattices with opposite magnetization, lattice A for the spin-up projection and B for the spin-down projection as depicted in Fig. 7. Since the two sublattices are identical, despite of their opposite magnetization, it is sufficient to calculate the dynamics of only one sublattice and obtain those of the other through the symmetry $G_{A,\sigma} = G_{B,-\sigma}$. The self-consistency condition for the Bethe lattice reads

$$\Delta_{A(B),\sigma}(t,t') = v(t)G_{B(A),\sigma}(t,t')v^*(t')$$

and using the symmetry it becomes

$$\Delta_\sigma(t,t') = v(t)G_{-\sigma}(t,t')v^*(t').$$

3.2 Time-dependent electric field

Applying an unpolarized AC electric field to the system, which is propagating in the z direction results in a time-periodic linear potential originating from the root of the Bethe lattice via a driving term

$$H_{drv}(t) = \sum_j eaE_0 \sin(\omega t)s_j n_j, \tag{14}$$

with the electric charge e, the strength of the field E_0, the angular frequency of the driving ω and s_j the number of steps from the root of the tree to site j. Performing the unitary transformation

$$U(t) = e^{i\phi(t)\sum_j s_j n_j},$$

where $\phi(t) = -(eaE_0/\omega)\cos(\omega t)$, the full Hamiltonian $H(t) = H_{Hubbard} + H_{drv}(t)$ can be transformed into the rotating-frame Hamiltonian

$$
\begin{aligned}
H_{rot}(t) &= i\frac{dU(t)}{dt}U^\dagger(t) + U(t)H(t)U^\dagger(t) \\
&= -i\sum_l eaE_0\sin(\omega t)s_l n_l e^{(i\phi(t)\sum_l s_l n_l)}e^{(-i\phi(t)\sum_k s_k n_k)}+ \\
&\quad e^{i\phi(t)\sum_l s_l n_l}\Big(-\sum_{\langle i,j\rangle,\sigma}t_{ij}d_{i\sigma}^\dagger d_{j\sigma}+\sum_i U(d_{i\uparrow}^\dagger d_{i\uparrow}-\frac{1}{2})(d_{i\downarrow}^\dagger d_{i\downarrow}-\frac{1}{2})+ \\
&\quad \sum_i eaE_0\sin(\omega t)s_i n_i)e^{-i\phi(t)\sum_k s_k n_k} \\
&= -\sum_l eaE_0\sin(\omega t)s_l n_l e^{\phi(t)\sum_l s_l n_l}e^{i\phi(t)\sum_k s_k n_k}+ \\
&\quad e^{i\phi(t)\sum_l s_l n_l}i\sum_l eaE_0\sin(\omega t)s_l n_l e^{i\phi(t)\sum_k s_k n_k} + (1+i\phi(t)\sum_l s_l n_l + ...)\times \\
&\quad -\sum_{\langle i,j\rangle,\sigma}t_{ij}d_{i\sigma}^\dagger d_{j\sigma}\times -(1+i\phi(t)\sum_k s_k n_k + ...) + (1+i\phi(t)\sum_l s_l n_l + ...)\times \\
&\quad -\sum_i U(d_{i\uparrow}^\dagger d_{i\uparrow}-\frac{1}{2})(d_{i\downarrow}^\dagger d_{i\downarrow}-\frac{1}{2})\times -(1+i\phi(t)\sum_k s_k n_k + ...) \\
&= eaE_0\sin(\omega t)s_k \times e^{\phi(t)\sum_l s_l n_l}e^{i\phi(t)\sum_k s_k n_k}\times\sum_{l\neq k}eaE_0\sin(\omega t)s_l n_l\times(1-1)+ \\
&\quad e^{-i\phi(t)s_k}e^{i\phi(t)s_l}\times -\sum_{\langle i,j\rangle,\sigma}t_{ij}d_{i\sigma}^\dagger d_{j\sigma}\times e^{i\phi(t)\sum_{k\neq i,j}s_k n_k}e^{-i\phi(t)\sum_{l\neq i,j}s_l n_l}+ \\
&\quad e^{-i\phi(t)s_i}e^{i\phi(t)s_i}\times -\sum_i U(d_{i\uparrow}^\dagger d_{i\uparrow}-\frac{1}{2})(d_{i\downarrow}^\dagger d_{i\downarrow}-\frac{1}{2})\times \\
&\quad e^{i\phi(t)\sum_{k\neq i}s_k n_k}e^{-i\phi(t)\sum_{l\neq i}s_l n_l}
\end{aligned}
$$

This results in the elimination of the driving term. The rotating frame Hamiltonian H_{rot} and $H_{Hubbard}$ differ only by a time-dependent Peierls phase on the hopping amplitude

$$t_{ij}(t) = t_0 e^{iA(s_i - s_j)\cos(\omega t)}. \tag{15}$$

The factor $(s_i - s_j) = \pm 1$ implies nearest neighbor hopping and we define the dimensionless driving amplitude as $A = eaE_0/\omega$.

3.3   Floquet Theory

Since we are studying periodically driven systems, we want to give a short overview of the Floquet formalism (for recent reviews see [30, 31]), which originates from the general theorem [32] for differential equations $dx(t)/dt = C(t)x(t)$, with C periodic in t. For a quantum system, whose dynamics are determined by the Schrödinger equation

$$i\frac{d}{dt} \mid \psi(t)\rangle = H(t) \mid \psi(t)\rangle, \tag{16}$$

with $H(t + \mathcal{T}) = H(t)$ and the period of the time-dependent Hamiltonian $\mathcal{T} = 2\pi/\omega$. The Floquet theorem states, that there is a solution to the Schrödinger equation of the form

$$\mid \psi(t)\rangle = e^{-i\epsilon_\alpha t} \mid \psi_\alpha(t)\rangle$$

$$\mid \psi_\alpha(t)\rangle = \mid \psi_\alpha(t + \mathcal{T})\rangle,$$

with the eigenvalues of the time translation $e^{-i\epsilon_\alpha t}$, where α is a set of quantum numbers and the quasi-energies ϵ_α lie within $-\omega/2 < \epsilon_\alpha \leq \omega/2$. By expanding the Floquet states $\mid \psi_\alpha(t)\rangle$ in terms of Floquet modes $\mid \psi_{\alpha,m}(t)\rangle$

$$\mid \psi_\alpha(t)\rangle = \sum_m e^{-im\omega t} \mid \psi_{\alpha,m}\rangle,$$

we can Fourier transform Eq. (16) to

$$(\epsilon_\alpha + m\omega) \mid \psi_{\alpha,m}\rangle = \sum_{m'} H_{m-m'} \mid \psi_{\alpha,m'}\rangle,$$

in terms of the Fourier components of the Hamiltonian

$$H_m = \frac{1}{\mathcal{T}} \int_0^{\mathcal{T}} dt e^{im\omega t} H_{rot}(t).$$

For the Hubbard model with time-dependent hopping the Fourier components are [33]

$$H_m = -t_0 \sum_{<i,j>} (-1)^m \mathscr{J}_m \left((s_i - s_j)A \right) d_i^\dagger d_j + \delta_{m,0} U \sum_j n_{j\uparrow} n_{j\downarrow},$$

so the hopping is renormalized by the mth Bessel function $\mathscr{J}_m \left((s_i - s_j)A \right)$ and the Coulomb interactions survives only for the $m = 0$ sector.

Bukov et al. [34] have shown that it is possible to perform a Schrieffer-Wolff transformation to a periodically driven, strongly interacting Fermi-Hubbard model using Floquet theory and a high frequency expansion. This is particularly useful in the resonant driving regime, where the driving frequency is a multiple of the Hubbard interaction, because an effective Hamiltonian with doublon creation and annihilation processes can be derived. The Schrieffer-Wolff transformation and the high-frequency expansion can be placed on equal footing because they both rely on the concept that virtual high energy states can be replaced by dressed low energy ones. We will give a short review of the derivation in [34] and extend it by adding the coupling to the fermionic bath.

Considering the undriven Hamiltonian (1) in the strongly correlated regime $t_0 \ll U$, one can go to the rotating frame $| \psi^{rot}(t) \rangle = V(t)^\dagger | \psi(t) \rangle$ with the operator $V(t) = e^{-iUt \sum_j n_{j\uparrow} n_{j\downarrow}}$, where the Coulomb interaction is replaced by an oscillating term. The Schrödinger equation (16) is then

$$i \frac{d}{dt} | \psi^{rot}(t) \rangle = H^{rot}(t) | \psi^{rot}(t) \rangle,$$

with

$$H^{rot}(t) = -t_0 \sum_{<i,j>,\sigma} [g_{ij\sigma} + (e^{iUt} h_{ij\sigma}^\dagger + h.c.)],$$

$$h_{ij\sigma}^\dagger = n_{i\bar\sigma} d_{i\sigma}^\dagger d_{j\sigma} (1 - n_{j\bar\sigma}),$$

$$g_{ij\sigma} = (1 - n_{i\bar\sigma}) d_{i\sigma}^\dagger d_{j\sigma} (1 - n_{j\bar\sigma}) + n_{i\bar\sigma} d_{i\sigma}^\dagger d_{j\sigma} n_{j\bar\sigma},$$

where $\bar\uparrow = \downarrow$ and vise versa. The term g_{ij} corresponds to doublon and holon hopping processes and $h_{ij\sigma}^\dagger$ to the creation and annihilation of doublon-holon pairs between the sites i and j. Since $H^{rot}(t)$ is $2\pi/U$-periodic, one can apply Floquet's theorem and perform a high frequency expansion for $H^{rot}(t) = \sum_l H_l^{rot} e^{ilUt}$, which results in the effective Hamiltonian [35, 36, 37]

$$H_{eff} = H_0^{rot} + \sum_{l>0} \frac{[H_l^{rot}, H_{-l}^{rot}]}{lU} + O(1/U^2).$$

To generalize the high frequency expansion to periodically driven systems Bukov et al.

extend the Hamiltonian to

$$H_{Hubbard} = -t_0 \sum_{\langle i,j \rangle, \sigma}^{N} d_{i\sigma}^{\dagger} d_{j\sigma} + U \sum_{i}^{N} n_{i\uparrow} n_{i\downarrow} + \sum_{j,\sigma} f_{j,\sigma}(t) n_{j,\sigma},$$

where the last term $\sum_{j,\sigma} f_{j,\sigma}(t) n_{j,\sigma}$ corresponds to the driving Hamiltonian H_{drv} (see (14)) in the previous subsection 3.2. Their work is limited to $t_0 \ll U, \omega$ and it is assumed that the amplitude of the field is scaled with ω. Going to the rotating frame now requires a transformation with the operator $V(t) = e^{-iUt \sum_j n_{j\uparrow} n_{j\downarrow} + \sum_{j,\sigma} F_{j,\sigma}(t) n_{j,\sigma}}$, where $F_{j,\sigma}(t) = \int_0^t f_{j,\sigma}(t') dt'$. This induces a phase shift to the hopping as we saw in Eq. (15) and the rotating frame Hamiltonian including the periodic driving reads as

$$H^{rot}(t) = -t_0 \sum_{<i,j>,\sigma} [e^{i\delta F_{ij\sigma}(t)} g_{ij\sigma} + (e^{i[Ut + \delta F_{ij\sigma}(t)]} h_{ij\sigma}^{\dagger} + h.c.)],$$

with $\delta F_{ij\sigma}(t) = F_{i\sigma}(t) - F_{j\sigma}(t)$. Since we are working with a Bethe lattice exposed to the driving $f_{j,\sigma}(t) = eaE_0 \sin(\omega t) s_{j,\sigma}$, the phase of the hopping is $\delta F_{ij\sigma}(t) = A(s_i - s_j) \cos(\omega t)$ with $A = eaE_0/\omega$ (see subsection (3.2)).

For nonresonant driving the application of the Schrieffer-Wolff-Transformation yields to the suppression of double occupancies and the leading term is $H_{eff}^{(1)}$, whereas in the resonant driving regime $t_0 \ll U = l\omega$ the zeroth order term

$$H_{eff}^{(0)} = \sum_{<i,j>,\sigma} \left\{ -J_{eff} g_{ij\sigma} - K_{eff} \left[(-1)^{l\eta_{ij}} h_{ij\sigma}^{\dagger} + h.c. \right] \right\} \tag{17}$$

dominates with $\eta_{ij} = 1$ for $i > j$, $\eta_{ij} = 0$ for $i < j$ and the renormalized coefficients

$$J_{eff} = t_0 \mathscr{J}_0(A),$$

$$K_{eff} = t_0 \mathscr{J}_l(A),$$

where $\mathscr{J}_l(A)$ denotes the lth Bessel function. The strength of the parameters J_{eff} and K_{eff} can be manipulated through the driving amplitude, which gives rise to novel physics. It was recently found that tuning an AC field such that $J_{eff} < 0$, can flip the band structure and therefore turn an repulsive interaction to an attractive one [38]. Through the absorption of resonant drive photons doublon-holon pairs can form, which are dynamical degrees of freedom of the system. For $K_{eff} > J_{eff}$ the dynamics are dominated by doublon-holon creation and annihilation processes and for $K_{eff} < J_{eff}$ by the hopping of doublon-holon pairs. For an amplitude of the driving field such that $K_{eff} = J_{eff}$ and l even, the doublon-holon creation is equal to the hopping rate, which modifies a strongly interacting fermionic system into an effectively noninteracting one.

To take account for the energy dissipation between system and bath, we will now extend the above derivation to a periodically driven system which is coupled to a fermionic bath. The full Hamiltonian is

$$H = -t_0 \sum_{\langle i,j \rangle, \sigma}^{N} d_{i\sigma}^{\dagger} d_{j\sigma} + U \sum_{j}^{N} n_{j\uparrow} n_{j\downarrow} + \sum_{j,\sigma} f_{j,\sigma}(t) n_{j,\sigma} + \sum_{k,\sigma} \varepsilon_k b_{k,\sigma}^{\dagger} b_{k,\sigma} + \sum_{j,k,\sigma} (V_k b_{k,\sigma}^{\dagger} d_{j,\sigma} + h.c.),$$

(18)

where the last two terms describe the bath energies H_{fBath} and the coupling between the system and its environment H_{fMix}. If we assume, that the coupling to the dissipation bath V_k is small we can treat H_{fMix} as a perturbation to the system and evaluate the tunneling rate between the system and the bath. The full Hamiltonian is the unperturbed Hubbard Hamiltonian including the dissipation term

$$H = H_{Hubbard} + H_{fMix}$$

$$H_{fMix} = \sum_{j,k,\sigma} (V_k b_{k,\sigma}^{\dagger} d_{j,\sigma} + h.c.),$$

with the coupling V_k, which can vary from 0 (no perturbation) to 1 (full perturbation). The total tunneling rate W is given to first order in perturbation by

$$W = \sum_{\langle i,j \rangle, k, k', \sigma} W_{i,j,k,k',\sigma} = 2\pi \sum_{\langle i,j \rangle, k, k', \sigma} \rho \mid H_{i,j,k,k',\sigma} \mid^2,$$

(19)

with the density matrix ρ of the unperturbed system (for the derivation see [39]). This gives rise to two sorts of terms

$$\sum_{\langle i,j \rangle, k, k', \sigma} \mid H_{i,j,k,k',\sigma} \mid^2 = \sum_{\langle i,j \rangle, k, k', \sigma} (V_k V_{k'}^* b_{k,\sigma}^{\dagger} b_{k',\sigma} d_{j,\sigma} d_{i,\sigma}^{\dagger} + h.c.) + (V_k V_{k'} b_{k,\sigma}^{\dagger} b_{k',\sigma}^{\dagger} d_{j,\sigma} d_{i,\sigma} + h.c.).$$

(20)

The terms in the second bracket do not commute with the particle number operator

$$\sum_{i,j,\sigma} [d_{j,\sigma} d_{i,\sigma}, n_{i\sigma}] \neq 0$$

, so they will be omitted from the total Hamiltonian such that $[H, N] = 0$ assuring that the system preserves particle number. Performing the transformation to the rotating frame with the operator $V(t) = e^{-iUt \sum_j n_{j\uparrow} n_{j\downarrow} + \sum_{j,\sigma} F_{j,\sigma}(t) n_{j,\sigma}}$ to the first term on the r.h.s. of Eq. (20)

25

gives the tunneling rate in the rotating frame

$$W^{rot}(t) = 2\pi \sum_{\langle i,j \rangle, k, k', \sigma} \rho V_k V_{k'}^* \left\{ e^{i\delta F_{ij\sigma}(t)} b_{k,\sigma}^\dagger b_{k',\sigma} g_{ij\sigma} + (e^{i[Ut+\delta F_{ij\sigma}(t)]} b_{k,\sigma}^\dagger b_{k',\sigma} h_{ij\sigma}^\dagger + h.c.) \right\}.$$

In a second step we again calculate the zeroth-order, period averaged contribution obtained from the high frequency expansion and arrive at

$$W_{eff}^{(0)} = 2\pi \sum_{\langle i,j \rangle k, k', \sigma} \rho \left\{ J_{eff}^{bath} b_{k,\sigma}^\dagger b_{k',\sigma} g_{ij\sigma} + K_{eff}^{bath} ((-1)^{l\eta_{ij}} b_{k,\sigma}^\dagger b_{k',\sigma} h_{ij\sigma}^\dagger + h.c.) \right\}$$

with the renormalized bath hopping parameters $J_{eff}^{bath} = V_k V_{k'}^* \mathcal{J}_0(A)$ and $K_{eff}^{bath} = V_k V_{k'}^* \mathcal{J}_l(A)$. Supposedly the tunneling rate between the system and heat bath can be described through the doublon and holon hopping g_{ij} and the creation and annihilation of doublon pairs $h_{ij\sigma}^\dagger$.

3.4   Dissipation

A system, which is attached to a fermionic bath with a bilinear structure, can be integrated out analytically. It turns out that it contributes to the system through an additional self-energy correction. The Dyson equation can be symbolically written as

$$\underline{G}(t,t') = (\underline{G}_0^{-1}(t,t') - \underline{\Sigma}_{fBath}(t,t') - \underline{\Sigma}(t,t'))^{-1}, \tag{21}$$

where all objects are matrices and the bath self-energy is given by

$$\Sigma_{fBath}^{\alpha\alpha}(t,t') = \sum_\beta G^{\beta\beta}(t,t') \times \Lambda_\beta^{\alpha\alpha}(t,t')$$

with the bath hybridization function

$$\Lambda_\beta^{\alpha\alpha}(t,t') = \langle \alpha \mid d_\sigma \mid \beta \rangle \langle \beta \mid d_\sigma^\dagger \mid \alpha \rangle \Delta_\sigma^<(t,t') + \langle \alpha \mid d_\sigma^\dagger \mid \beta \rangle \langle \beta \mid d_\sigma \mid \alpha \rangle \Delta_\sigma^>(t,t'),$$

defined via the coupling densities $\Gamma(\omega) = \pi \sum_k V_k V_k^* \delta(\omega + \mu_k - \epsilon_{k,\sigma})$ and the initial occupation given by the Fermi Dirac distribution analogous to (6):

$$\Delta^<(t,t') = \int_{-\infty}^\infty \frac{d\omega}{\pi} e^{-i\omega(t-t')} \Gamma(\omega) f(\omega - \mu)$$

and

$$\Delta^>(t,t') = \int_{-\infty}^\infty \frac{d\omega}{\pi} e^{-i\omega(t-t')} \Gamma(\omega)(1 - f(\omega - \mu)).$$
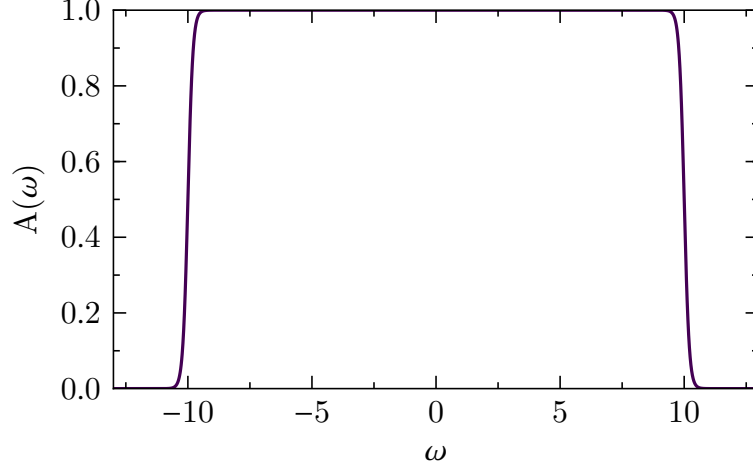
Figure 9: Flat density of states with a soft cutoff is chosen for the coupling densities of the fermionic heat bath.

The simplest treatment of the dissipation is to chose $\Gamma(\omega)$ to be a flat density of states with a soft cutoff $\Gamma(\omega) = \frac{\Gamma}{(1+e^{\nu(\omega-\omega_c)})(1+e^{-\nu(\omega+\omega_c)})}$ as represented in 9. We chose $\Gamma\nu = 10$ and the band cutoff energy $\Gamma\omega_c = 10$, while holding the chemical potential at $\mu = 0$. As illustrated in Fig. 6 each site is attached to its own reservoir with a coupling strength Γ.

3.5 Physical observables

The observable we are interested in measures the energy that flows between the system and the heat bath and can be obtained from $I_E(t) = \langle \mathcal{I}_E(t) \rangle$. The energy current $\mathcal{I}_E(t)$ is defined as

$$\mathcal{I}_E = \dot{H}_{fBath} = i[H, H_{fBath}] + \frac{\partial H_{fBath}}{\partial t},$$

with $H = H_D + H_B + H_{hyb} + H_{fBath} + H_{fMix}$ describing the original Anderson impurity Hamiltonian (4). This leads to

$$\mathcal{I}_E = i[\sum_{k,\sigma}(V_k f_{k,\sigma}^\dagger d_\sigma + V_k^* d_\sigma^\dagger f_{k,\sigma}), \sum_{k',\sigma'} \varepsilon_{k'} f_{k',\sigma'}^\dagger f_{k',\sigma'}]$$

$$= i\sum_{k,\sigma}(V_k f_{k,\sigma}^\dagger d_\sigma + V_k^* d_\sigma^\dagger f_{k,\sigma})\varepsilon_k f_{k,\sigma}^\dagger f_{k,\sigma} - i\sum_{k,\sigma} \varepsilon_k f_{k,\sigma}^\dagger f_{k,\sigma}(V_k f_{k,\sigma}^\dagger d_\sigma + V_k^* d_\sigma^\dagger f_{k,\sigma})$$

$$= i\sum_{k,\sigma} \varepsilon_k (V_k d_\sigma f_{k,\sigma}^\dagger - V_k^* f_{k,\sigma} d_\sigma^\dagger).$$

The energy current operator can be obtained by summing over all diagrams that have a

27

special hybridization line that places the current operator at the tip of the Keldysh contour

$$I_E(t) = \int_0^t d\tau \Delta_f^<(t, \tau) G^<(t, \tau),$$

with the energy hybridization function $\Delta_f^<(t, \tau) = \int_{-\infty}^{\infty} \frac{d\omega}{\pi} e^{-i\omega(t-\tau)} \omega \Gamma(\omega) f(\omega - \mu)$.

3.6 Numerical implementation

Working with nonequilibrium systems involves explicit time dependence. In order to solve the impurity problem, we need to solve Dyson equations of the form

$$\underline{G}(t, t') = \underline{G}^{(0)}(t, t') - \int_0^t dt_1 \int_0^{t_1} dt_2 \underline{G}^{(0)}(t, t_1) \underline{\Sigma}(t_1, t_2) \underline{G}(t_2, t') \tag{22}$$

and

$$\underline{K}(t, t') = \underline{K}^{(0)}(t, t') + \int_0^t dt_1 \int_0^{t'} dt_2 \underline{K}(t_1, t_2) \underline{\Delta}(t_1, t_2) \underline{G}^\dagger(t, t_1) \underline{G}(t', t_2). \tag{23}$$

Here $\underline{G}(t, t')$ and $\underline{K}(t, t')$ denote the bold propagators and correlation functions described in subsection 2.4.2 in the matrix notation. These are two-dimensional Volterra integral equations, as indicated by the integral limits. We project Eq. (22) and (23) onto a time grid with N_t time slices and $t_i = i\Delta t$ nodes, where $i \in \{0, 1, ..., N_t - 1\}$ and $\Delta t = t_{max}/(N_t - 1)$ with the maximum simulation time t_{max}. The discretized version of the above equations reads

$$\underline{G}(t_i, t_j) = \underline{G}^{(0)}(t_i, t_j) - (\Delta t)^2 \sum_{k=0}^{t_i} \sum_{l=0}^{t_k} \underline{G}^{(0)}(t_i, t_k) \underline{\Sigma}(t_k, t_l) \underline{G}(t_l, t_j) w_{ik} w_{jl}$$

and

$$\underline{K}(t_i, t_j) = \underline{K}^{(0)}(t_i, t_j) + (\Delta t)^2 \sum_{k=0}^{t_i} \sum_{l=0}^{t_j} \underline{K}(t_k, t_l) \underline{\Delta}(t_k, t_l) \underline{G}^\dagger(t_i, t_k) \underline{G}(t_j, t_l) w_{ik} w_{jl}.$$

We compute every time-slice t_i by starting with $\underline{G}(t_i, t_j = t_i)$ or $\underline{K}(t_i, t_j = t_i)$ and successively increasing/decreasing t_j depending on whether we want to fill in the upper/lower triangle of the matrix. The integration weights are chosen to be

$$w_{2,j} = \begin{cases} 1/3 & j = 0, 2 \\ 4/3 & j = 1 \end{cases}$$

for $i = 2$ and

$$w_{i,j} = \begin{cases} 2/3 & j = 0, i \\ 7/24 & j = 1, i - 1 \\ 1/6 & j = 2, i - 2 \\ 1/24 & j = 3, i - 3 \\ 1 & 4 \leq j \leq i - 4 \end{cases}$$

for $i \geq 3$.

4 Results

In this chapter we will present the numerical results obtained for a dissipative Hubbard model driven by a periodic electric field. The aim is to develop tools which can help us understand and control the effect of electron-electron interactions on the energy flow between the system and its environment, the systems distribution function and spectral properties. All results consider a particle-hole symmetric system starting from a perfect anti-ferromagnetic state $(U \rightarrow \infty)$ with a quench to a finite Coulomb interaction U at $t = 0$.

We start out discussion in section 4.1 for a system which is not coupled to a dissipation bath and study the effect that periodic driving has on the magnetic relaxation. This allows for the comparison to existing publications [40] and reduces the computational time since the hybridization to the fermionic heat bath does not enter the calculations. Section 4.2 treats the effect of the driving field on the energy flow between the system and bath. All results are obtained for $k_B = \hbar = a = 1$.

4.1 Magnetic relaxation in a periodically driven Hubbard model

Before exploring new phenomena, we want to ensure that we can reproduce already known physics. In their recent research Martin Eckstein and al. [40] studied the melting of long-range antiferromagnetic order in a periodically driven repulsive Hubbard model starting from the Néel state and performing a quench to a finite U at $t = 0$. This chapter is orientated on their work and reproduces a part of the results, where in a first step the melting in the absence of a driving field is investigated and in a second step the effect of a strong driving field with a resonant frequency is explored. In as well as out of equilibrium the system is closed. The two quantities we are focusing on are the double occupation $d(t) = < n_\uparrow(t)n_\downarrow(t) >$, which is measuring the formation of charge excitations and the magnetization $M(t) = \frac{<n_\uparrow(t)-n_\downarrow(t)>}{1-2d(t)}$ as an indicator for the antiferromagnetic order of the the system. The magnetization $M(t)$ is formed by the staggered magnetic order parameter, which is normalized by the probability of a site being singly occupied. We are calculating the dynamics with nonequilibrium DMFT for a Bethe-lattice in infinite dimensions and comparing them to those in their paper [40], which are obtained with a matrix product impurity solver. The solid lines in Fig. 10 and 11 represent our results within the NCA and the dotted lines the exact ones, which converge at short times. Even though the NCA cannot reproduce the exact numbers for the observables, it is a reasonable approximation for high Coulomb interactions and has the advantage of a low computational cost.

4.1.1 Undriven magnetic melting

To begin with, we will differentiate the melting mechanisms for different regimes in the undriven case ($A = 0$, $v = v_0 = 1$). In the Mott-insulating regime with a strong Coulomb interaction $U \gg v$, Fig. 10 shows the magnetic order parameter $M(t)$ and the double occupation $d(t)$ for different values of U during the time range $0 \leq v_0 t \lesssim 6$. The dynamics of both observables start with oscillations at short times $v_0 t \simeq 1$ resulting from the Néel state not being an eigenstate of the Hubbard model at finite U. The formation of charge excitations relaxes rapidly to a U dependent steady state value at a low rate since the strong Coulomb interaction is preventing electrons from hopping across the lattice and the magnetization $M(t)$ exhibits a linear decrease with a U dependent gradient. The fast relaxation of the charge dynamics compared to the magnetization indicates that the magnetic melting is due to the movement of the charge excitations on top of the anti-ferromagnetic spin background.

To further underpin this statement Eckstein et al. investigated the spin precession dynamics by flipping an initially located fermion at a single probe site in the x direction. An effective magnetic field B_{eff}, which is formed by the neighboring sites, is orientated along the z direction leading to harmonic precession of the magnetic moment in the $x - y$ plane. It turns out that the precessing magnetic moment is sustained, even for times $v_0 t > 1$, which confirms that the decay of the magnetic order is due to mobile charge excitations and local magnetic moments are preserved.
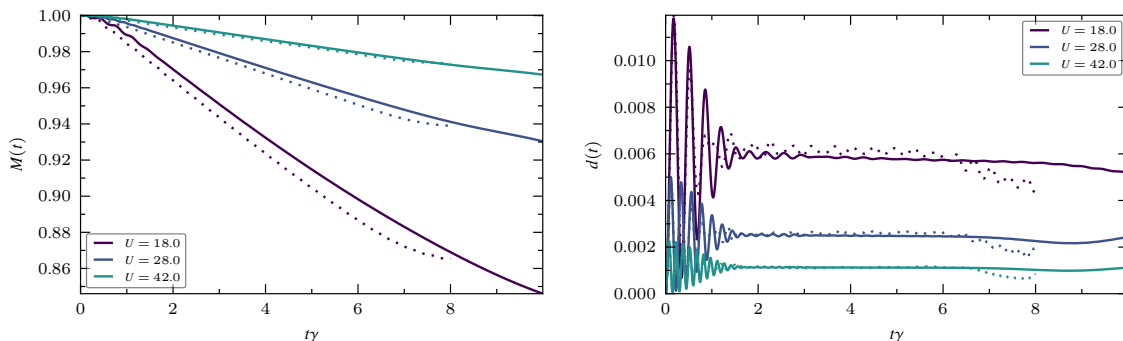

Figure 10: Dynamics of the system without driving for high Coulomb interactions $U \gg 1$. Left side: Decay of magnetic order parameter $M(t)$. Right side: Decay of double occupation $d(t)$. In both cases the solid lines represent the calculations obtained from the NCA and the dotted lines are the comparison to the extact results in [40]. .

When the Coulomb interaction is lowered, approaching the noninteracting limit $U = 0$, one expects quasiparticles to be responsible for the dynamics of the system. For $U \lesssim 1$ the magnetization shows an oscillatory behavior and decays to zero rapidly, while $d(t)$ relaxes to high values [40]. Compared to the results for $U \gg v$, where the spin dynamics relax much slower than the charge dynamics, here $M(t)$ and $d(t)$ both relax around $v_0 t \simeq 1$, indicating
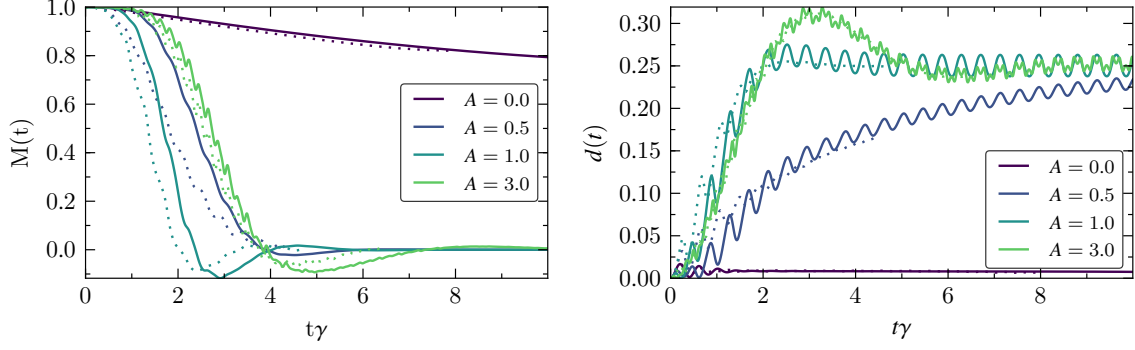
Figure 11: Dynamics of the system with $U = \omega = 15$ and various amplitudes. Left side: Decay of magnetic order parameter $M(t)$. Right side: Decay of double occupation $d(t)$. The solid lines represent the calculations obtained from the NCA and the dotted lines are the comparison to the extact results in [40].

that the destruction of the anti ferromagnetic order is caused by the destruction of local magnetic moments.

4.1.2 Magnetic melting in resonant driven lattices

Martin Eckstein et al explored the effects of an electric driving field in three different regimes: the high frequency, the resonant and the in gap away from resonant driving regime. In Fig. 11 we are reproducing the magnetic melting for the case of resonant driving, which modifies the behavior of $M(t)$ and $d(t)$ strongly, changing the magnetization from a slow decay in the absence of driving to a fast decay even for small driving amplitudes. The double occupation goes from a saturation at low values to high values resembling the case for $U \lesssim 1$. Thus, resonant driving is a tool to switch from the charge-excitation to the quasiparticle melting mechanism and control the relaxation speed of the charge and spin dynamics.

It strikes that for $A = 2, 3$ the double occupation exceeds the value of the noninteracting limit $d = 0.25$. This can be understood from the effective Hamiltonian (17) with $l = 1$. For $A = 0.5, 1.0$ the dynamics are dominated by electron/holon hopping processes because $K_{eff} < J_{eff}$, whereas for $A = 3$ doublon/holon creation processes dominate explaining why the double occupation increases. The appearance of $d > 0.25$ was observed before for a high frequency drive and large amplitudes, which causes a flipping of the sign of the hopping and therefore an effective attractive interaction [38].

32

4.2 System-bath energy dissipation in a periodically driven Hubbard model

This chapter discusses the system's ability to dissipate energy into a fermionic heat bath while it is constantly driven out of equilibrium by an AC electric field, referred to as the pump or driving field. We are considering a Bethe lattice in the limit of infinite coordination number Z and hopping $t_0 = v_0/Z$, where our numerical approach is exact (subsection 3.1), coupled to a fermionic bath, which is a flat band with a soft cutoff as discussed in subsection 3.4 with the coupling $\Gamma = 0.5$ and $\omega_c = 10$. The system is subjected to an unpolarized AC electric field along the z direction $E(t) = A*\cos(\omega t)$, where $A = eaE_0/\omega$ is the dimensionless driving amplitude. In the following we set $e, a = 1$ and use v_0 as the unit of energy. The energy current between the system and the thermal bath is measured by the current operator described in subsection 3.5. To ascertain the frequencies at which the dissipation takes place, we are applying an additional second electric field, referred to as the probe field, with a small field amplitude of $A_{\text{probe}} = 0.05$, that does not change the state of the system. Its purpose is to probe the system's response, which is the amount of energy that it dissipated into the bath as a result of the perturbation. In equilibrium, we expect the response to be linear. We are discussing a system with $U = 10$ corresponding to a Mott insulator with a bandgap of $\Delta_{gap} = U - 2*\frac{D}{2} = 6$, where D is half the bandwidth and Mott-like system with $U = 5$ without a defined bandgap, where the competition between the kinetic and potential energy starts to play a role. The driving field to which the system is exposed to has a driving frequency of $\omega_{pump} = U$, referred to as the the resonant $l = 1$ regime and $\omega_{pump} = U/2$, the half-resonant $l = 2$ regime.

Both electric fields enter the mathematical equations as described in Ch. 3.2. The system's response $P_{\omega_{\text{probe}}}(A_{\text{probe}})$ to the probe field is measured by the derivative of the energy current, which is defined in Ch. 3.5, with respect to the probe amplitude $A_{\text{probe}}(\omega_{\text{probe}})$

$$
\begin{aligned}
P_{\omega_{\text{probe}}}(A_{\text{probe}}) &= \lim_{A_{\text{probe}} \to 0} \frac{dI_E(A_{\text{probe}}(\omega_{\text{probe}}))}{dA_{\text{probe}}(\omega_{\text{probe}})} \simeq \frac{I_E(\Delta A_{\text{probe}}(\omega_{\text{probe}}))}{\Delta A_{\text{probe}}(\omega_{\text{probe}})} \\
&= \frac{I_E(A_{\text{probe}}(\omega_{\text{probe}})) - I_E(A_{\text{probe}=0}(\omega_{\text{probe}}))}{A_{\text{probe}}(\omega_{\text{probe}}) - A_{\text{probe}=0}(\omega_{\text{probe}})}.
\end{aligned}
\tag{24}
$$

An example of the energy current and the double occupation of the system in Fig. 12 shows oscillations with the frequency ω_{pump} and the emergence of a steady state after $t \simeq 2$. The same applies for the response $P_{\omega_{probe}}$ and therefore from now on we are interested in the period averaged values of those observables. We are taking the $\mathcal{T}$-averaged response $\overline{P}_{\omega_{\text{probe}}}$
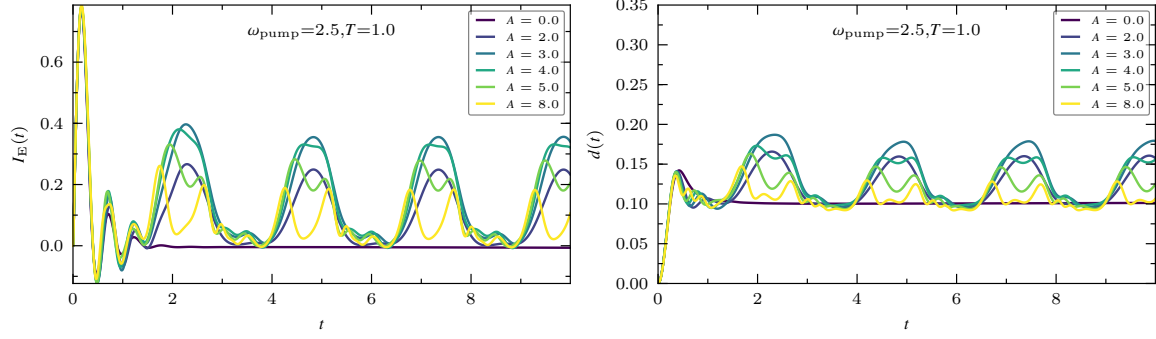
Figure 12: Time-dependent heat current (left panel) between the system and the fermionic bath, induced by a half-resonant ($\omega_{\text{pump}} = 2.5$) driving field with different amplitudes and double occupation (right panel).

$$\overline{P}_{\omega_{\text{probe}}}(t) = \frac{1}{\mathcal{T}} \int_0^{\mathcal{T}} ds P_{\omega_{\text{probe}}}(t, t - s)$$

to estimate the amount of energy that is flowing into the heat bath as a result of the probing.

In equilibrium ($A = 0$) there is an energy flow to the bath only for times $t \leq 2$, resulting from the quench to a finite U at $t = 0$. Turning on the driving field induces a grow in energy dissipation for field strengths up to $A = 3$ in the half-resonant regime and $A = 2$ in the resonant regime, after which the energy current starts to decrease again indicating a nonlinear behavior, which we will further examine in the following chapters.

Another part of our analysis will be to investigate spectral properties of the system as the $\mathcal{T}$-averaged spectral function

$$\overline{A}(\omega) = -\frac{1}{\pi} Im \overline{G}^R(\omega)$$

$$\overline{G}^R(\omega) = \frac{1}{\mathcal{T}} \int_0^{\mathcal{T}} dt \int_0^t ds \exp^{i\omega s} G^R(t, t - s)$$

and the nonequilibrium distribution from Eq. 9

$$F(\omega, t) = \frac{Im G^<(\omega, t)}{2\pi A(\omega, t)}$$

with $A(\omega, t)$ and $G(\omega, t)$ given by the partial Fourier transform (7). The $\mathcal{T}$-averaged electronic distribution function is obtained from

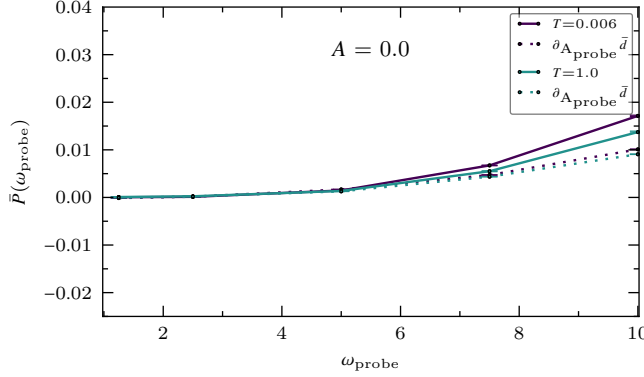$$\overline{F}(\omega) = \frac{Im \overline{G}^<(\omega)}{2\pi \overline{A}(\omega)}.$$

Figure 13: Averaged energy flow $\overline{P}_E$ between system and heat bath generated by a probe pulse at different frequencies ω_{probe} for a system in equilibrium. The bath is kept at $T = 0.006$ and $T = 1.0$ respectively.

4.2.1 High U regime

We will start our discussion by looking at the response of an undriven lattice with the Coulomb interaction $U/t_0 = 10, t_0 = 1$ corresponding to a system in the Mott insulating regime. Probing at different frequencies starts to generate a response only for $\omega_{\text{probe}} \geq 5 = U/2$ as seen in Fig. 13. Hence, probing with frequencies lying within the width of the Hubbard bands and below the bandgap does not change the dissipation to the bath or the double occupation of the system. The transfer of energies $\omega_{\text{probe}} \geq U/2$ promotes an electron to cross the bandgap, thereby creating a doubly occupied site next to an empty site - a doublon-hole pair. This increases the doublon density as well as the energy current to the fermionic bath, in which an excited electron is hopping to the bath and another electron with the energy difference $\Delta\omega$ is hopping back to the lattice. Interestingly, a system coupled to a bath with $T = 0.006$ is more sensitive to perturbations then $T = 1.0$, although in general systems at lower temperatures are more static and therefore have a lower double occupation.

Half-resonant driving

Driving the system with $\omega_{pump} = \frac{U}{2}$ changes the response $\overline{P}_{\omega_{probe}}$ due to a probe pulse with the amplitude $A_{probe} = 0.05$ drastically: A strong deviation from equilibrium, even for small amplitudes, occurs at $\omega_{pump} = \omega_{probe} = \frac{U}{2}$ as seen in Fig. 14. As the system transitions into a nonequilibrium state, we expect the energy flow to the bath to grow in order to balance the injected energy from the pump field, which proofs to be true (see Fig. 12), although a nonlinear amplitude dependent behavior is observed. A similar nonlinear effect can be seen for the response at energy $\omega_{probe} = 5$. With increasing strength of the pump field the system's response grows linearly for small amplitudes ($A \leq 2$), followed by a downwards trend resulting in a negative response for most amplitudes. The energy dissipation for the
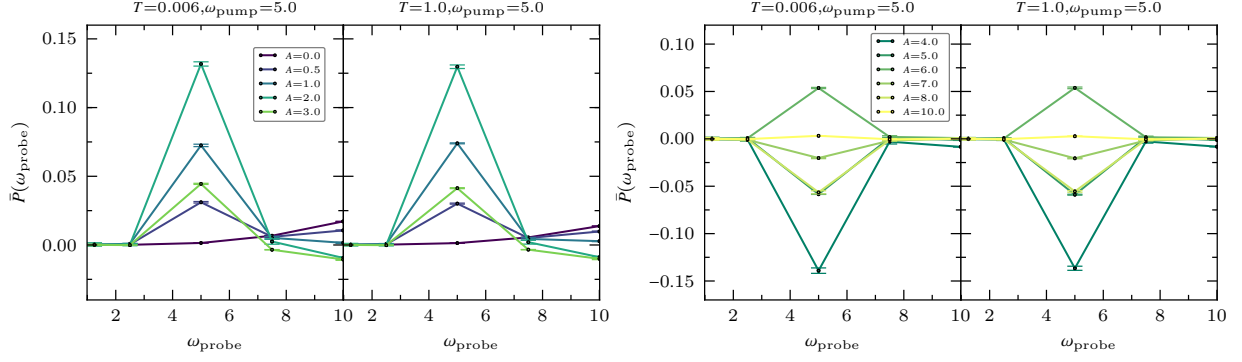
Figure 14: Response $\overline{P}_E$ generated by a probe field at different frequencies ω_{probe} while the system is constantly driven at $U/2 = \omega_{\mathrm{pump}} = 5.0$ and an increasing field strength A.
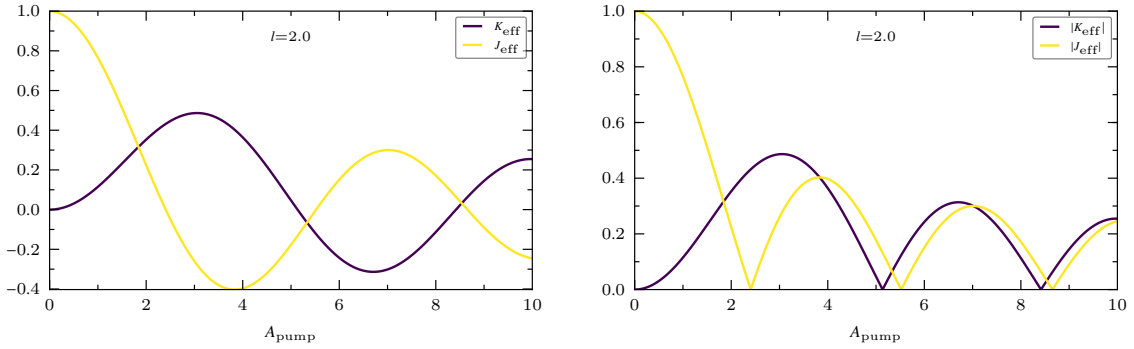

Figure 15: Driving amplitude dependence of the doublon-holon creation parameter K_{eff} and hopping J_{eff} in the resonant $l = 2$ regime on the left side and its absolute value on the right side.

$\omega_{probe} = 10$ channel immediately decreases and drops to negative values for $A < 1 \leq 5$, after which it remains resistant to perturbations at higher driving amplitudes. It is not intuitively understood why for specific frequencies some driving amplitudes promote energy dissipation, while others suppress or even cause a decrease of energy flow as a response to the probe field.

To gain more insight to the origin of this intriguing behavior, we need to investigate the observables describing the system in the nonequilibrium steady state. There is a correlation between the system's period-averaged double occupation $\overline{d} = \frac{1}{\mathcal{T}} \int_0^{\mathcal{T}} dt < n_\uparrow(t) n_\downarrow(t) >$ and energy current $\overline{I}_E = \frac{1}{\mathcal{T}} \int_0^{\mathcal{T}} dt I_E(t)$ between system and bath (see Fig. 16). Both show a similar amplitude dependence, where an increase of the doublon density coincides with an increase of the energy dissipation and vice versa, while the total electron density remains constant. The same counts for the field-strength dependent response $\overline{P}_{\omega_{probe}}$ at $\omega_{probe} = 5$ and $\omega_{probe} = 10$ examined in Fig. 17 and the change of the doublon density $\partial_{A_{probe}} \overline{d}$, which is obtained analogously to the response via Eq. 24.

The amplitude dependence of the doublon density can be understood through a closer

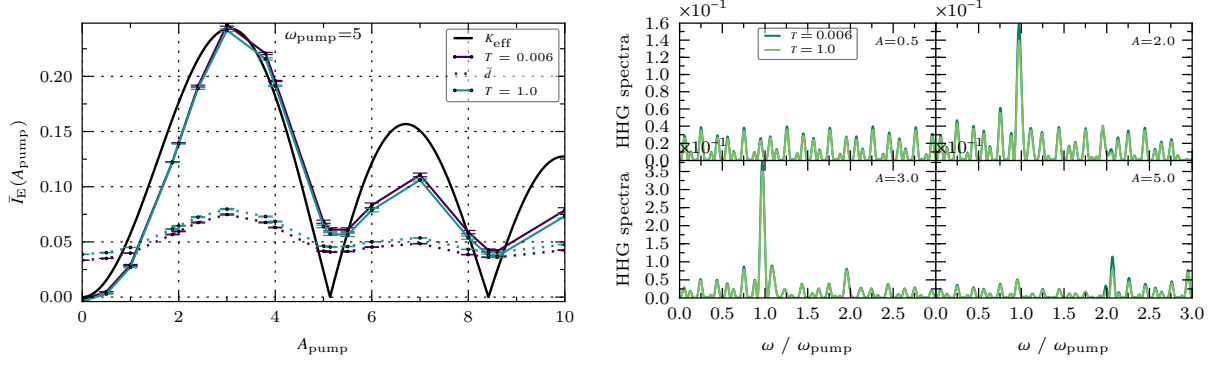Figure 16: Left: Field-strength dependence of energy current $\overline{I}_E$ between system and fermionic heat bath averaged over the period $2\pi/\omega_{\text{pump}}$ in the $l = 2$ regime with $U = 10, \omega_{\text{pump}} = 5$. The dotted lines display the period-averaged doublon density $\overline{d} = < \overline{n_\uparrow n_\downarrow} >$ and the black line the doublon-holon creation parameter K_{eff} in units of the coupling to the heat bath $\Gamma = 0.5$. Right: High harmonic spectroscopy of light-induced energy current $I_E(t)$.

look at the doublon/holon creation K_{eff} and hopping rate J_{eff} in Eq. 17. The results in subsection 4.1.2 show that as predicted an isolated, periodically driven system in the resonant $l = 2$ regime can be mapped to the noninteracting limit, if $K_{eff} = J_{eff}$. An open system does not exhibit this effect, since the double occupation never exceeds the value $d = 0.25$, but Fig. 16 shows that it qualitatively follows the doublon/holon creation rate $|K_{eff}|$, peaking whenever A_{pump} matches a value that maximizes $|K_{eff}|$. For driving amplitudes at which $K_{eff}(A_{pump}) = 0$ the double occupation and the current decrease, but do not go back to the equilibrium value $\overline{d}(A_{pump} = 0)$. Still, the driving amplitude can be used as a tool to create doublon/holon pairs and therefore control the energy current between system and bath, which satisfies $\overline{I}_E(A_{pump}) \approx V_{bath}\frac{(\overline{d}(A_{pump})-\overline{d}(0))}{\overline{d}(0)}$, with the bath hopping $V_{bath} = \Gamma^2$. This indicates that the formation of doublon-hole pairs by resonant absorptions of driving photons promotes an electron with the energy ω to hop to the heat bath and another electron with the energy $\omega - \Delta\omega$ to hop back to the lattice, thus ejecting the energy $\Delta\omega$ into the bath. This observation aligns with the theoretical predictions we made in subsection 3.3, where we derived the tunneling rate between system and dissipation bath performing a transformation to the rotating frame and a high frequency expansion. It shows that the tunneling depends on the creation/annihilation and hopping rates of doublons/holons pairs, with the the rescaled parameters $K_{eff}^{bath} = \Gamma^2 K_{eff}$ and $J_{eff}^{bath} = \Gamma^2 J_{eff}$.

The right panel in Fig. 16 shows the harmonic emission spectrum in terms of ω/ω_{pump}, evaluated from the square of the Fourier transform of $\frac{d}{dt}I_E(t)$ as $I_{hh}(\omega) = |\omega I_E(\omega)|^2$, which is proportional to the power radiated at the given frequency [41, 42]. Here we use $I_E(\omega) = \frac{1}{\mathcal{T}}\int_0^{\mathcal{T}} d\bar{t}e^{i\bar{t}\omega}I_E(t)$. At low driving amplitudes the emission spectrum is spread evenly through-

out the frequency space. Increasing the doublon/holon creation rate K_{eff} by ramping up the amplitude, enhances emissions at $m * \omega_{pump}, m \in \mathbb{Z}$, confirming that energy is transferred to the bath through the recombination of an mth nearest neighbor doublon-holon pair for even m. The emission at $m = 1$ for amplitudes which intensify K_{eff}, stems from one-photon absorptions that excite electrons from the lower Hubbard band to states around $\omega = 0$. Since in a Mott insulator there are no available states at this energy range, the absorbed energy is directly transferred to the bath.

To understand why a weak perturbing field alters the amount and direction of energy flow between the system and its environment so strongly, involves a more complex interplay between J_{eff} and K_{eff} and in particular their change $\partial_{probeA}K_{eff}$, $\partial_{probeA}J_{eff}$ due to the probing field. The change of the rates is calculated as

$$\partial_{probeA}K_{eff} = (K_{eff}(A_{pump} + A_{probe}) - K_{eff}(A_{pupmp}))/A_{probe}.$$

Fig. 17 shows the amplitude dependent response with respect to the equilibrium value $\overline{P}_{\omega_{\text{probe}}}(A_{pump}) - \overline{P}_{\omega_{\text{probe}}}(0)$ for a single frequency together with the scaled change of the doublon density $\partial_{A_{probe}}\overline{d}(A_{pump}) - \partial_{A_{probe}}\overline{d}(0)$. Similarly to Fig. 16 this reveals that whenever the doublon density increases/decreases the same change appears for the energy current because there are more/less recombinations of doublon-hole pairs. Comparing the response for the probe frequency $\omega_{probe} = 5$ in the lower left panel of Fig. 17 to the change of the doublon creation $\partial_{probeA}J_{eff}$ and hopping rate $\partial_{A_{probe}}K_{eff}$ on top, shows that whenever they balance each other out $|\partial_{A_{probe}}K_{eff}| = |\partial_{A_{probe}}J_{eff}|$ (for $A_{pump} \cong 3.5, 5.1, 6.8, 8.4$), the system's response is suppressed. Driving amplitudes for which $|\partial_{A_{probe}}K_{eff}| < |\partial_{A_{probe}}J_{eff}|$ cause an increase of the energy dissipation in the $l = 2$ regime, where K_{eff} is repulsive, because the hopping of doublon/holon pairs becomes less favorable then the creations/recombinations. The reverse process is responsible for the negative response whenever $|\partial_{A_{probe}}K_{eff}| > |\partial_{A_{probe}}J_{eff}|$, where the creation of doublon/holons is lowered. Since an energy $\omega_{pump} = 5$ is constantly absorbed, which creates doublons at an energy cost of U, probing the system at $\omega_{probe} = U = 10$, destructs doublon/holon pairs and therefore less energy is dissipated to the bath.

Resonant driving

From the correspondence between the energy current $\overline{I}_E$ and the doublon creation/annihilation rate K_{eff} in Fig. 19 we can deduce, that driving with the same frequency as the Coulomb interaction $U = \omega_{pump} = 10$ enables a more precise control of the dissipation between system and bath then driving in the $l = 2$ regime, with the possibility of totally suppressing the energy current and bringing the double occupation close to its equilibrium value $\overline{d}(A_{pump} = 0)$, whenever A_{pump} matches values suppressing K_{eff}. This indicates that in the $l = 1$ regime
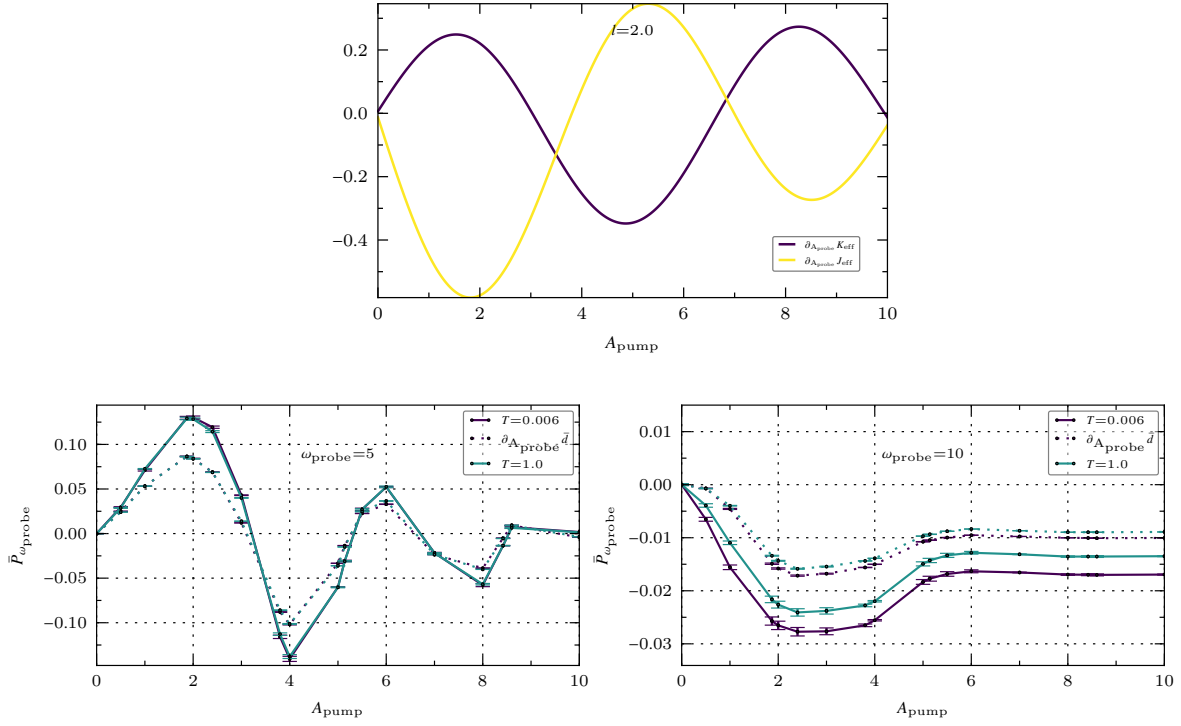
38

Figure 17: Upper: Change of doublon-holon creation parameter K_{eff} and hopping J_{eff} as a response to a probe field in the $l = 2$ regime. Lower: Solid lines correspond to the change of the period-averaged energy current with respect to the equilibrium value as a function of the driving amplitude and dotted lines to the change of the scaled double occupancy $\partial_{A_{probe}}\overline{d}(A_{pump})/v_{bath}$ with respect to the equilibrium value $\partial_{A_{probe}}\overline{d}(0)$ generated by a probe pulse at frequency $\omega_{\text{probe}} = 5$ and $\omega_{\text{probe}} = 10$.

the dissipation is entirely governed by the creation of doublons and holons, which is plausible since an energy that is needed for the creation of doublons/holons is constantly pumped into the system. Examining the harmonic spectrum (left panel in Fig. 19) underlines this statement, because it exhibits strong emissions $\omega = m * \omega_{pump}$ in the $m = 1$ and $m = 2$ sector, with weaker emissions at larger m.
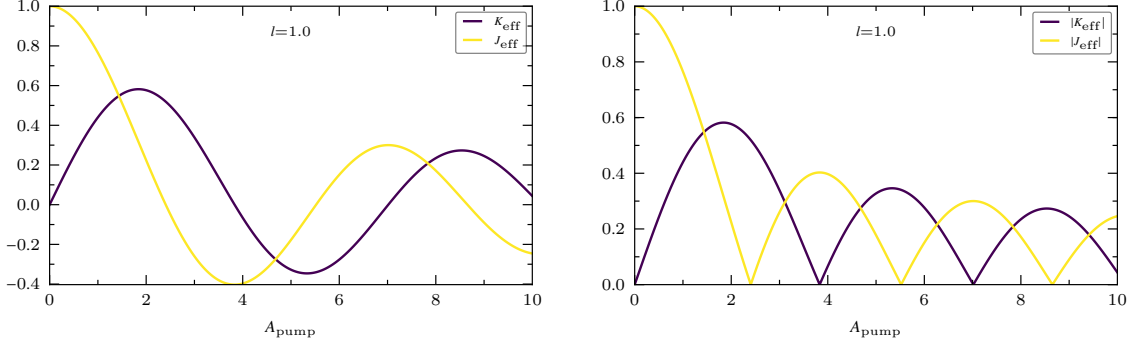

Figure 18: Driving amplitude dependence of the doublon-holon creation parameter K_{eff} and hopping J_{eff} in the resonant $l = 1$ regime on the left side and its absolute value on the right side.
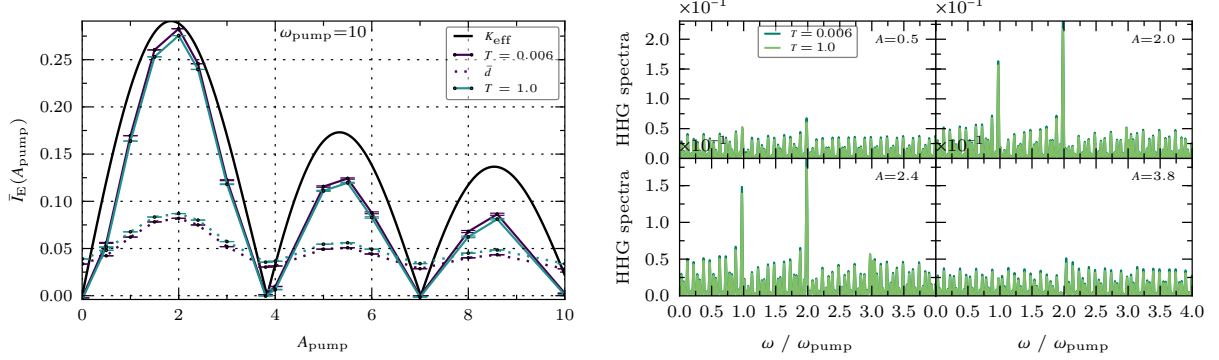

Figure 19: Left: Field-strength dependence of energy current $\overline{I}_E$ averaged over the period $2\pi/\omega_{\mathrm{pump}}$ in the $l = 1$ regime with $U = \omega_{\mathrm{pump}} = 10$. The dotted lines display the period-averaged doublon density $\overline{d} = < \overline{n_\uparrow n_\downarrow} >$ and the black line the doublon-holon creation parameter in units of the coupling to the heat bath $\Gamma = 0.5$. Right: High harmonic spectroscopy of light-induced energy current $I_E(t)$.

Since an energy $\omega = 10$ is constantly absorbed and emitted due to the driving, this turns out to be the frequency which is most sensitive to the probing. The lower panel of Fig. 20 shows that opposing to the $l = 2$ regime, where special amplitudes giving $|\partial_{A_{probe}} K_{eff}(A_{pump})| = |\partial_{A_{probe}} J_{eff}(A_{pump})|$ lead to a suppression of the response at $\omega_{probe} = \omega_{pump}$, driving in the $l = 1$ regime generates a maximum/minimum response depending on the

signs of the parameters. The cancellation of the parameters with equal signs causes a maximal increase of the doublon density, whereas the opposite applies for $\partial_{A_{probe}} K_{eff}(A_{pump}) = -\partial_{A_{probe}} J_{eff}(A_{pump})$, where the creation of doublons and holons becomes less favorable.

Probing at $\omega_{probe} = 5$ (lower left panel in Fig. 20) always results in a negative response, although the amount of dissipated energy is altered only minimally. It strikes that the change of the energy current and the doublon density are not correlated, which indicates that a different dissipation mechanism is present. In fact, $\overline{P}_{\omega_{probe=5.0}}(A_{pump})$ follows $|\partial_{A_{probe}} J_{eff}(A_{pump})|$, so we can assume that doublon/holon hopping processes play an important role. The spectral functions in Fig. 21 show that a spectral weight for low energy states grows not only for an electric field with $\omega_{pump} = U/2$, but also for $\omega_{pump} = U$, enabling doublons to move around the lattice when the frequency of the probe field is $\omega_{probe} = 5$ instead of transferring it to the bath.
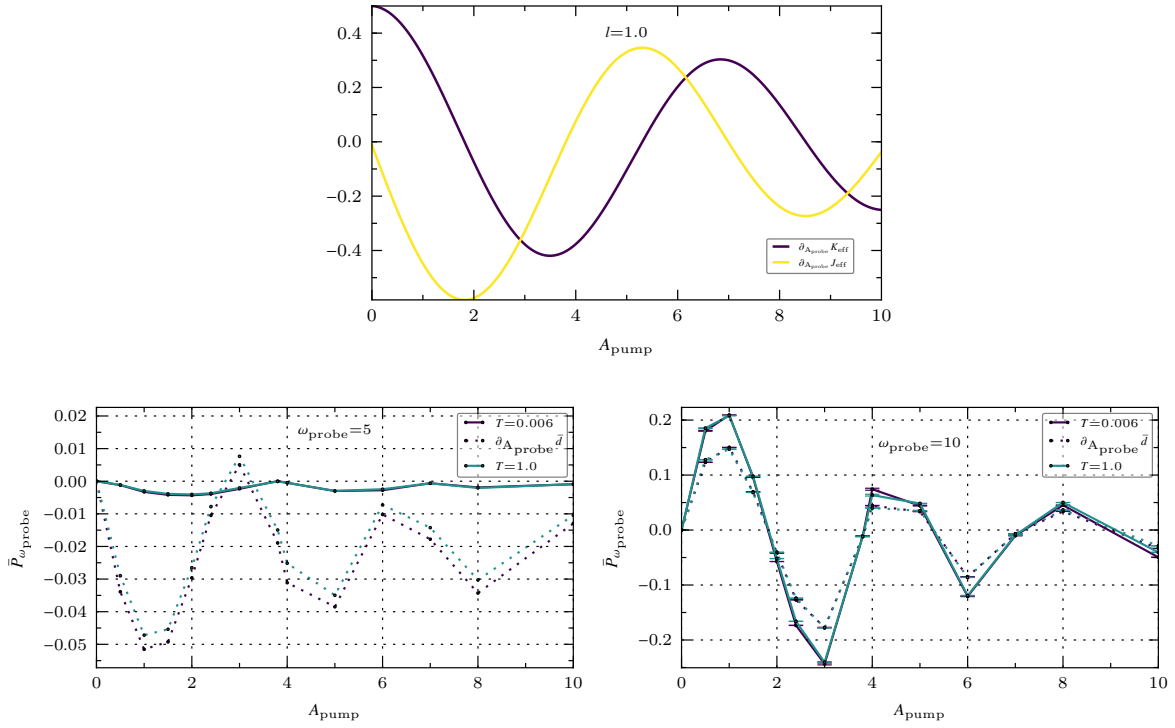

Figure 20: Upper: Change of doublon-holon creation parameter K_{eff} and hopping J_{eff} as a response to a probe field in the $l = 1$ regime. Lower: Solid lines correspond to the change of period-averaged energy dissipation as a function of the driving amplitude and dotted lines to the change of double occupancy $\partial_{A_{probe}} \bar{d}(A_{\text{pump}})//v_{bath}$ generated by a probe pulse at frequency $\omega_{\text{probe}} = 10$.

Spectral properties

We are further exploiting how the spectral properties of the system change due to the driving. In Fig. 21 both, the period-averaged $|\uparrow\rangle$-electronic spectral function and the period- and spin-
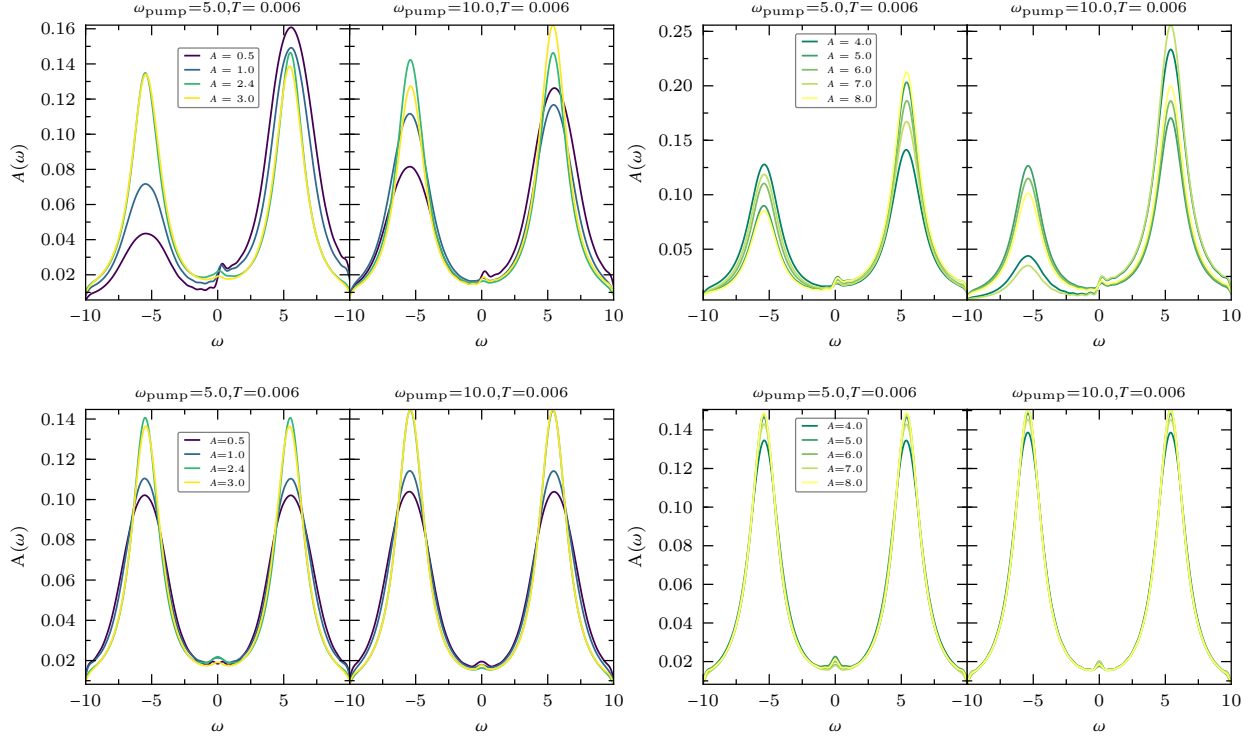
Figure 21: Upper: Comparison of period-averaged $|\uparrow\rangle$-electronic spectral functions for the $l = 1$ ($\omega_{pump} = U = 10$) and $l = 2$ ($\omega_{pump} = U/2 = 5$) regime with increasing field amplitude and a bath temperature kept at $T = 0.006$. Lower: Period- and spin-averaged spectral functions.

averaged spectral functions are illustrated for various driving amplitudes A_{pump} in the two different driving regimes. A small spectral weight grows around $\omega = 0$ when the AC field is turned on, creating metallic states in an insulating system of correlated electrons. As the intensity of the field is increased the bands become sharper, because electrons are excited towards states around $\omega = \pm 5$, but the spectrum does not split into a Wannier stark ladder. Hence, there is no dynamical localization as seen for other periodically driven systems where ω_{pump} is much smaller then U [43].

The spin dependent spectral functions exhibits a strong imbalance between the lower and the upper Hubbard band especially in the undriven case, which makes sense since the high Coulomb interaction prevents electrons from hopping across the lattice. Starting from a $|\uparrow\rangle$-state the probability for available $|\downarrow\rangle$-states after a final time t will still be higher and the more rigid the system is the longer it will take for spectral functions with opposite spins to align. Driving amplitudes for which the rate of doublon creations K_{eff} is high lift this asymmetry and the probability of available states with an energy ω aligns for both spins. By averaging over both spin states the asymmetry is canceled out. All spectral functions satisfy Eq. 8 up to a numerical error.

To further endorse that the system's nonequilibrium behavior can be controlled through the amplitude of the electric field, we investigate the distribution functions for the two driving mechanisms at a bath temperature $T = 0.006$ and $T = 1.0$ in Fig. 22. In equilibrium $F(\omega)$ mimics the Fermi-Dirac distribution and we can see how it starts to deviate when the system is exposed to an electric field. The evolution of $F(\omega)$ indicates that the system's effective temperature rises up to a threshold A_{pump}, which corresponds

to the amplitude maximizing $K_{eff}(A_{pump})$ after which it drops again. The same way driving in the $l = 1$ regime with $\omega_{pump} = U = 10$ allowed to suppress the dissipation between the system and bath whenever $K_{eff}(A_{pump}) = 0$, the distribution function goes back to its equilibrium shape for those values. Hence, the same nonlinear amplitude dependence we detected for the heat current is present for the temperature. In the lower panel of Fig. 22 the spectral function $A(\omega)$ is plotted together with the occupation $N(\omega)$ (shaded region), which furthermore confirms that amplitudes maximizing the doublon creation rate K_{eff} pump most electrons from the lower band to states at $\omega = 5$ thereby increasing the effective temperature. This is in line with the propelled double occupation $\overline{d}(A_{pump})$ we saw in Fig. 16 and 19.

4.2.2 Intermediate U regime

For a Mott-like system with a decreased Coulomb interaction of $U = 5$, there is no pronounced bandgap anymore. Instead a spectral weight around $\omega = 0$ (see Fig. 26) is present and below a critical temperature, which is estimated by $k_B T_K = U\sqrt{\frac{\Gamma}{2U}}e^{-\frac{\pi U}{8\Gamma} + \frac{\pi\Gamma}{2U}} \approx 0.17$, we can even observe the characteristics of Kondo physics, where the spectral function forms a peak at $\omega = 0$. When an equilibrium system in the high U regime is probed, an increase of the double occupation comes along with an increase of the heat current (see Fig. 13), revealing that the dissipation mechanism is due to the creation of doublon pairs. This picture changes in a Mott-like system, where the probe field generates a high increase of $\partial_{A_{probe}}\overline{d}$ for $5 \leq \omega_{probe} \leq 7.5$, thus energies that excite an electron from the lower to the upper band. The response $\overline{P}_{\omega_{probe}}$ has a maximum at $\omega_{probe} = U + U/2 = 7.5$ and unlike the double occupation a clear temperature dependence, which indicates that the dissipation is not merely governed by the formation of doublons.

We want to point out that the approximation we are using is based on the assumption that the Coulomb interaction in our system is high, thus we are dealing with a Mott insulator. By lowering U the system enters a regime in which the kinetic and the potential energy start to compete and phase transitions occur, but the NCA may not give quantitatively reliable results. It can nevertheless be used as a tool to estimate qualitative results and map out the interesting parameter regimes, which then can be evaluated using more advanced methods, which we will address in the conclusions.
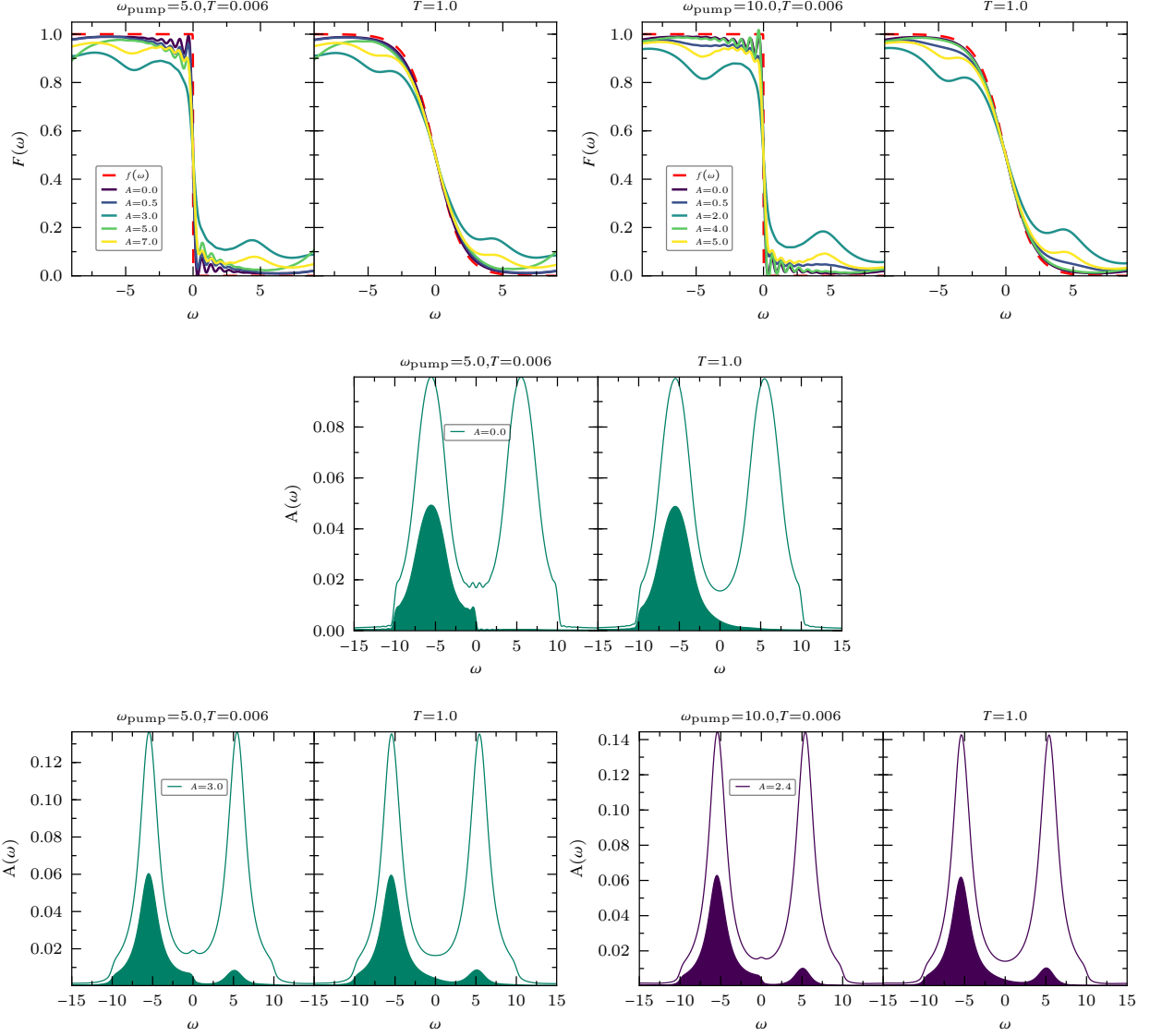
Figure 22: Upper: Nonequilibrium distribution functions for a system in two different driving regimes, coupled to a fermionic bath at $T = 0.006$ and $T = 1.0$. The red line corresponds to the Fermi-Dirac distribution. Lower: Spectral function $A(\omega)$ (thick line) and occupation $N(\omega)$ (shaded region) for an undriven system ($A = 0$) compared to a driven system with $A = 3.0$ in the $l = 2$ regime and $A = 2.4$ in the $l = 1$ regime. The comparison shows that specific amplitudes A induce an occupation inversion depending on the driving mechanism.
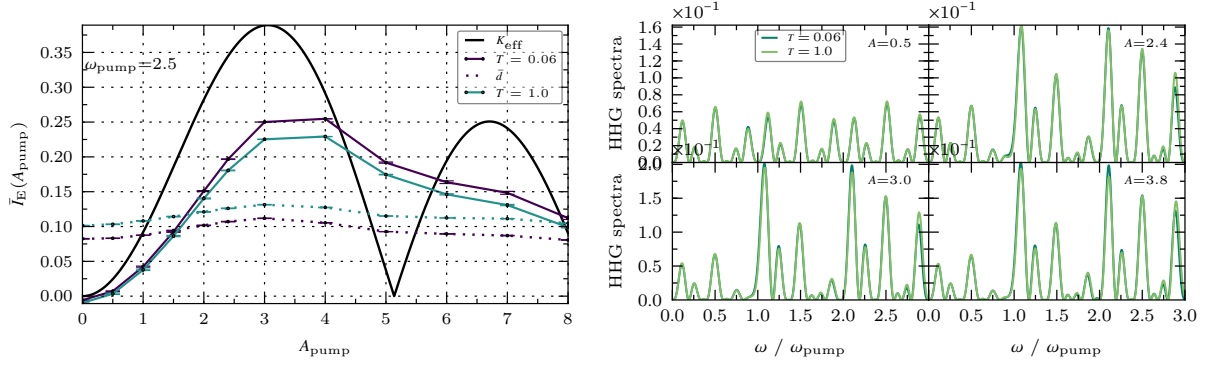
Figure 24: Field-strength dependence of energy current $\overline{I}_E$ averaged over the period $2\pi/\omega_{\text{pump}}$ in the $l = 2$ regime with $U = 5, \omega_{\text{pump}} = 2.5$. The dotted lines display the period-averaged doublon density $\overline{d} = <\overline{n_\uparrow n_\downarrow}>$ and the black line the doublon-holon creation parameter in units of the coupling to the heat bath $\Gamma = \sqrt{0.5}$.

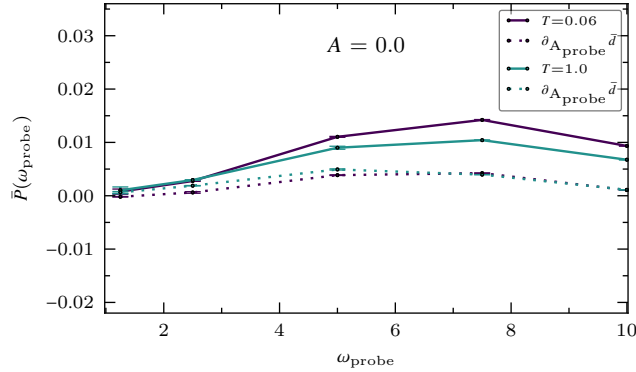Figure 23: Averaged energy flow $\overline{P}_E$ between system and heat bath generated by a probe pulse at different frequencies ω_{probe} for a system in equilibrium. The bath is kept at $T = 0.06$ and $T = 1.0$ respectively.

Half-resonant driving

Examining the amplitude dependence of the energy current and double occupation in Fig. 24 shows that for a system without a bandgap, the control of those parameters through the modulation of the driving amplitude becomes harder. Since there are available states around $\omega = U/2$, the driving regime cannot be clearly defined. Although the double occupation increases whenever K_{eff} goes up, there is no strict correlation between the current and the rate of doublon creations anymore. Therefore we can assume that additionally to the doublon creation rate the dissipation mechanism is governed by intra-band hopping processes, where electrons move around the lattice gaining kinetic energy, which is then transferred to the bath. This explains why the harmonic spectrum in Fig. 24 does not exhibit enhanced peaks at certain ω/ω_{pump} as we observed in the Mott insulating regime, but is rather similar to

45

Bloch oscillation type harmonics typical for a single tight binding model [44].
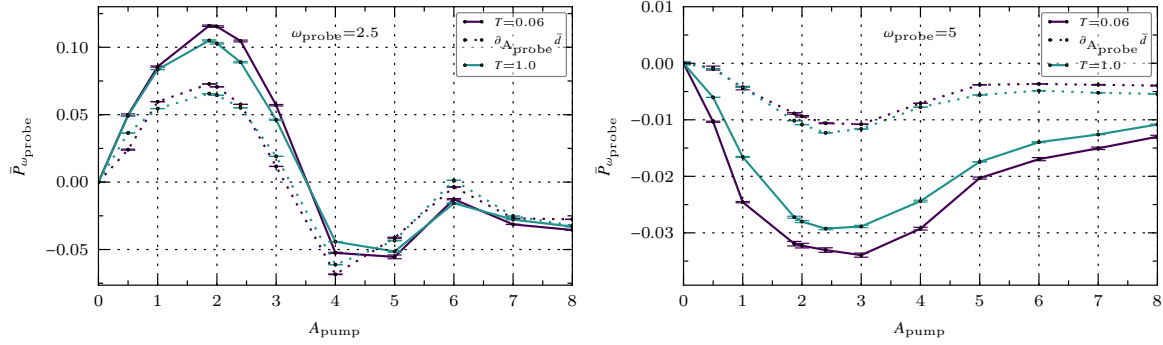

Figure 25: Solid lines correspond to the change of period-averaged energy dissipation as a function of the driving amplitude and dotted lines to the change of double occupancy $\partial_{A_{probe}}\bar{d}(A_{\text{pump}})//v_{bath}$ generated by a probe pulse at frequency $\omega_{\text{probe}} = 2.5$, and $\omega_{\text{probe}} = 5$.

Apparently, the temperature dependence of the the energy current $I_E(A_{pump})$ is interchanged compared to the double occupation $\bar{d}(A_{pump})$ with more current flowing to the bath at low temperatures, which is rather unintuitive. This is can be explained by the fact that energy emissions at $\Delta\omega = m * U + U/2$ are more likely for $T = 0.06$ because the spectral weight around $\omega = 0$ is higher (see Fig. 26).

The response in Fig. 25 again strongly deviates from equilibrium, especially for frequencies matching $\omega_{probe} = m * \omega_{pump}, m \in \mathbb{Z}$, since the electric field pumps electrons into the upper band at energies $\omega = 2.5$ (see Fig. 27). Although the energy current $\bar{I}_E$ does not show the same correlation to the doublon/holon creation rate K_{eff}, that was present in the Mott insulting regime, the response $\overline{P}_{\omega_{probe}}$ is strongly interwind with the change of the double occupation $\bar{d}(A_{pump})$ and both depend on $\partial_{A_{probe}}K_{eff}$ and $\partial_{A_{probe}}J_{eff}$ in the same manner as for $U = 10$: For the dissipation channel $\omega_{probe} = \omega_{pump} = 2.5$ the system's response is suppressed whenever $|\partial_{A_{probe}}K_{eff}| = |\partial_{A_{probe}}J_{eff}|$. Amplitudes for which $|\partial_{A_{probe}}K_{eff}| < |\partial_{A_{probe}}J_{eff}|$ increase the dissipation, while $|\partial_{A_{probe}}K_{eff}| > |\partial_{A_{probe}}J_{eff}|$ leads to a negative response. Probing at $\omega_{probe} = 2*\omega_{pump}$ annihilates doublon/holon pairs and therefore diminishes the dissipation.
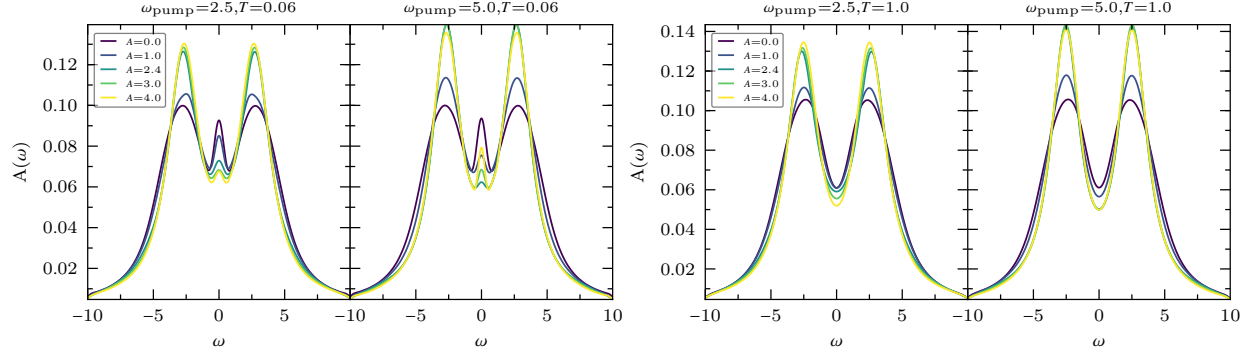
46

Spectral properties

Figure 26: Period- and spin-averaged spectral functions for a bath temperature $T = 0.06$ (left) and $T = 1.0$ (right) in the two different driving regimes with increasing field amplitude. For $T \leq T_K$ the emergence of a Kondo peak can be controlled through the amplitude depending on the driving regime.

In the previous subsection we showed that exposing a gapped system to an electric field increases the spectral weight in the mid gap region. Lowering U closes the gap such that electrons residing at $\omega = 0$ are excited to the upper and lower band. This leads to a reduction of low energy states and the creation of states around $\omega = \pm 2.5$ as seen in Fig. 26. A lattice is coupled to a bath below the critical Kondo temperature T_K forms a peak at $\omega = 0$ when no driving is applied. Although this peak is reduced by the field, it is possible to control its emergence through the driving amplitude, the same way it is possible to control the effective temperature of the system and its double occupation. Comparing the nonequilibrium distribution function for $\omega_{pump} = U = 5$ in Fig. 27 with the evolution of the Kondo peak indicates that whenever the amplitude of the field lowers the system's effective temperature, the peak is amplified and vice versa. The spectral functions and the occupations $N(\omega)$ (shaded region) for various amplitudes in Fig. 27 align with this picture. For $A = 0$ (upper right panel) there are no occupied states for $\omega > 0$ at $T = 0.06$, but when the field amplitude matches a value $A = 2$ that strongly increases the effective temperature, occupied states are shifted towards $\omega > 0$ and the occupations for $T = 0.06$ and $T = 1.0$ start to resemble. Ramping up the amplitude further to $A = 4.0$ has the opposite effect since the effective temperature is decreased again.
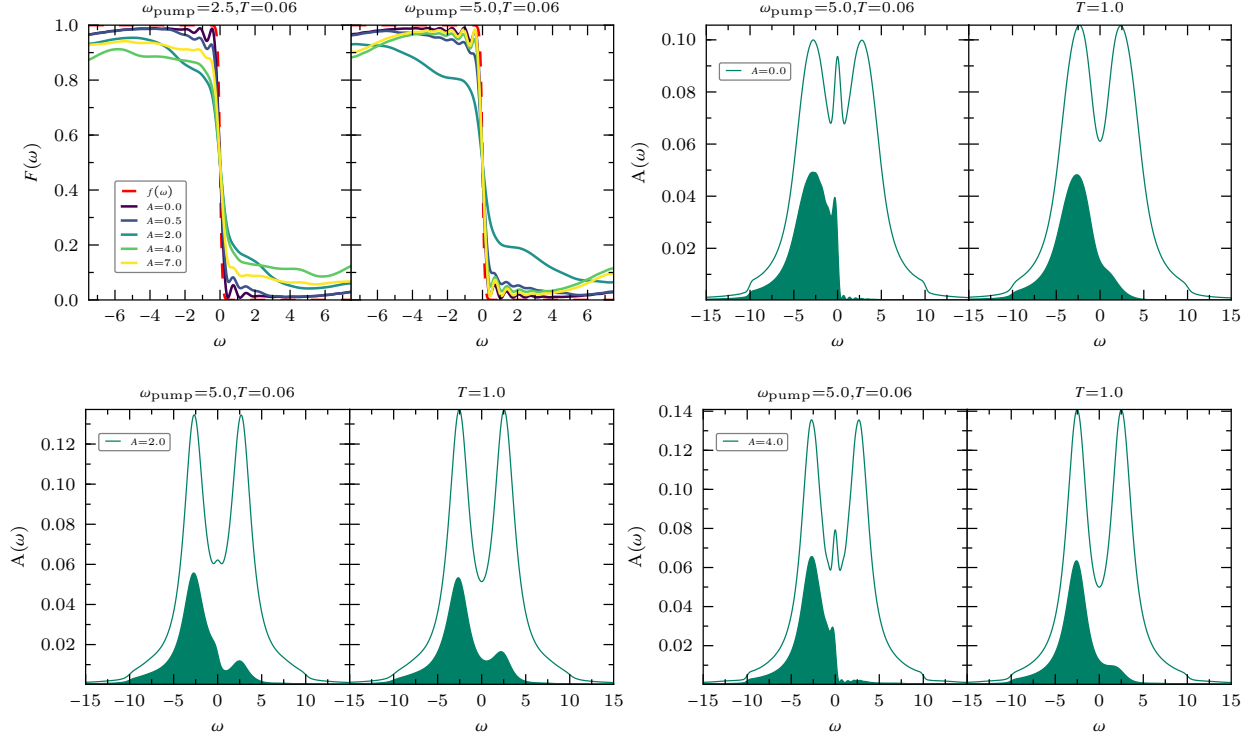
Figure 27: Upper left: Nonequilibrium distribution functions for a system in two different driving regimes, coupled to a fermionic bath at $T = 0.06$. The red line corresponds to the Fermi-Dirac distribution. Upper right: Spectral function $A(\omega)$ (thick line) and occupation $N(\omega)$ (shaded region) for an undriven system. Lower: Nonequilibrium spectral function and occupation for special amplitudes in the $l = 1$ regime with $\omega_{pump} = U = 5$, which maximize (left side) or minimize (right side) the effective temperature and double occupation.

5 Conclusion and outlook

In this thesis we developed tools to investigate and manipulate the nonequilibrium steady state of a dissipative Hubbard model driven by a periodic electric field. The dissipation is realized by coupling each lattice site to a noninteracting fermionic bath, which is in equilibrium and has a defined temperature. The focus of our studies lays on the energy current between system and bath, induced by the electric field, as well as the emergence of nonequilibrium distributions and density of states. The system was studied by means of dynamical mean field theory and the numerical implementation relies on the lowest order self-consistent hybridization expansion, which provides qualitatively reliable results in the Mott insulating regime.

Results were obtained for a system at half filling, which is initially in a perfect antiferromagnetic state and quenched to a finite U at time $t = 0$. The numerical setup was first tested in subsection 4.1 without the coupling to a fermionic heat bath. We could reproduce existing results [40], where periodic driving was used to control magnetic relaxation. In the absence of driving the relaxation depends on the ratio of the interaction to the hopping U/t_0. When $U \gg t_0$ the antiferromagnetic order decays due to mobile charge excitations and for $t_0 \gtrsim U$ it is governed by the dynamics of residual quasi-particles. Strong resonant driving with $\omega = U > t_0$ can be used as a tool to switch from the charge-excitation to the quasiparticle melting mechanism and control the relaxation speed of the charge and spin dynamics.

We then in subsection 4.2 went on to investigate how the system's ability to dissipate energy to a fermionic bath changes when it is driven by a periodic electric field. We started by looking at a gapped system with $U/t_0 = 10$ in equilibrium and saw that its response to a small perturbing field, which is the derivative of the heat current with respect to the amplitude of the probe field, is only given if the frequency of the probe field is large enough to promote electrons to cross the bandgap. Exposing the system to an electric field alters the response as well as the the energy current itself drastically. The drive was realized by either choosing the frequency of the electric field to correspond to the the bandgap $\omega_{pump} = U$ (resonant driving) or to $\omega_{pump} = U/2$ (half-resonant driving). In both cases we observed a correlation between the system's double occupation and dissipation current, which exhibit a nonlinear dependence on the driving amplitude. This can be explained following the work of Bukov et al. [34], where a Schrieffer-Wolff transformation was performed to derive an effective Hamiltonian, which describes the system's dynamics in terms of doublons and holons. We showed that the same transformation can be applied to the tunneling rate between the system and the heat bath, such that it can be expressed in terms of doublon/holon creation and annihilation as well as hopping processes with a rescaled bath hybridization, which depends on the amplitude of the

electric field. In both regimes tuning the amplitude enables the control of the energy current between the lattice and its environment, but for resonant driving this control turns out to be more precise and gives rise to possibility of completely suppressing the current whenever the driving amplitude matches a value that suppresses the creation of double occupied states. The response to a perturbing field is altered strongly when the system is driven out of equilibrium because of a complex interplay between the doublon/holon creation and hopping rate and their derivatives with respect to the probe field. We observed that whenever the doublon density increases/decreases when the system is probed, the same change appears for the energy current because there are more/less recombinations of doublon-hole pairs. In both regimes probing with the same frequency as the driving frequency can maximize the response or even lead to a negative response depending on the driving amplitude.

For a Mott-like system with a decreased Coulomb interaction of $U/t_0 = 5$, there is no pronounced bandgap and a spectral weight around $\omega = 0$ is present instead. Examining the amplitude dependence of the energy current and double occupation showed that the control of those observables through the modulation of the driving amplitude is more difficult. Since there are available states around $\omega = U/2$ the driving regime cannot be clearly defined. We assume that additionally to the doublon creation rate the dissipation mechanism is governed by intra-band hopping processes, where electrons move around the lattice gaining kinetic energy, which is then transferred to the bath.

We further went on to exploit how the spectral properties of both, the insulating ($U/t_0 = 10$) and the Mott-like ($U/t_0 = 5$) system, change due to the driving. We showed that exposing a gapped system to an electric field increases the spectral weight in the mid gap region, thereby creating metallic states in an insulating system of correlated electrons. As the intensity of the field is increased the bands become sharper, because electrons are excited towards states around $\omega = \omega_{pump}$. Lowering U closes the gap such that electrons residing at $\omega = 0$ are excited to the upper and lower band, which reduces low energy states. A lattice coupled to a bath below the critical Kondo temperature leads to the formation of a narrow spectral weight around $\omega = 0$ when no driving is applied. It is possible to control the emergence of the Kondo peak through the driving amplitude, the same way it is possible to control the system's double occupation. To further endorse that tuning the driving amplitude of the electric field works as a tool to manipulate the system's nonequilibrium behavior in a controlled manner, we investigated the nonequilibrium distribution functions $F(\omega)$ and occupations $N(\omega)$ for the insulating and the Mott-like system. The same nonlinear amplitude dependence we detected for the heat current is present for the temperature, as the evolution of $F(\omega)$ for various amplitudes reveals. The spectral functions $A(\omega)$ together with the occupation $N(\omega)$ furthermore confirmed that amplitudes maximizing the doublon creation rate pump electrons from the lower to the upper Hubbard band, thereby increasing the effective

temperature.

Within the scope of this work, we successfully implemented and tested our numerical method against existing results, but faced certain limitations which lead to the following open questions:

- The impurity solver we are using relies on the approximation that the Coulomb interaction is high and breaks down in regimes where the kinetic and potential energy are on the same scale or the system's temperature is below the critical Kondo temperature. A necessary step in order to describe regimes in which phase transitions occur, is to implement a numerically exact solver.

- We showed that the the energy current between the the system and its environment and its response to a small perturbing electric field is governed by the dynamics of doublons and holons. However, the effective Hamiltonian describing these processes is not trivial and a more detailed analysis of the electron pairing is required.

The here employed numerical setup can be extended to study a great amount of interesting systems and address further problems, such as:

- Instead of a Bethe lattice in the limit of infinite dimensions, a more realistic 2D or 3D lattice should be investigated.

- The main restriction of DMFT is that local correlations are described exactly only in the limit of infinite dimensions. In lower dimensions, where non-local correlations become more important, DMFT can be extended by mapping the lattice model to a cluster instead of a single-site.

- We examined a system in the one orbital case. Studying a multi orbital setup instead can lead to the understanding of more complex behaviors.

We plan to address the above mentioned open questions and implement the extensions in future projects.

References

[1] Martin Eckstein, Marcus Kollar, and Philipp Werner. Interaction quench in the hubbard model: Relaxation of the spectral function and the optical conductivity. *Physical Review B*, 81, 2010.

[2] Antoine Georges, Gabriel Kotliar, Werner Krauth, and Marcelo J Rozenberg. Dynamical mean-field theory of strongly correlated fermion systems and the limit of infinite dimensions. *Reviews of Modern Physics*, 68, 1996.

[3] Sidney Yip. *Handbook of materials modeling*. Springer Science & Business Media, 2007.

[4] Martin Eckstein and Philipp Werner. Nonequilibrium dynamical mean-field calculations based on the noncrossing approximation and its generalizations. *Physical Review B*, 82, 2010.

[5] Steven R White. Density matrix formulation for quantum renormalization groups. *Physical review letters*, 69, 1992.

[6] Jorgen Rammer. *Quantum transport theory*. CRC Press, 2018.

[7] Gerald D Mahan. *Many-particle physics*. Springer Science & Business Media, 2013.

[8] N Goldman, JC Budich, and P Zoller. Topological quantum matter with ultracold gases in optical lattices. *Nature Physics*, 12(7):639, 2016.

[9] Markus Greiner, Olaf Mandel, Tilman Esslinger, Theodor W Hänsch, and Immanuel Bloch. Quantum phase transition from a superfluid to a mott insulator in a gas of ultracold atoms. *nature*, 415(6867):39, 2002.

[10] Matteo Mitrano, Alice Cantaluppi, Daniele Nicoletti, Stefan Kaiser, A Perucchi, S Lupi, P Di Pietro, D Pontiroli, M Riccò, Stephen R Clark, et al. Possible light-induced superconductivity in k 3 c 60 at high temperature. *Nature*, 530(7591):461, 2016.

[11] Antoine Georges. A. georges, g. kotliar, w. krauth, and mj rozenberg, rev. mod. phys. 68, 13 (1996). *Rev. Mod. Phys.*, 68:13, 1996.

[12] John Hubbard. Electron correlations in narrow energy bands iii. an improved solution. *Proc. R. Soc. Lond. A*, 281, 1964.

[13] Junjiro Kanamori. Electron correlation and ferromagnetism of transition metals. *Progress of Theoretical Physics*, 30, 1963.

[14] Martin C Gutzwiller. Effect of correlation on the ferromagnetism of transition metals. *Physical Review Letters*, 10, 1963.

[15] Arti Garg, HR Krishnamurthy, and Mohit Randeria. Can correlations drive a band insulator metallic? *Physical review letters*, 97, 2006.

[16] Michele Fabrizio, Alexander O Gogolin, and Alexander A Nersesyan. From band insulator to mott insulator in one dimension. *Physical review letters*, 83, 1999.

[17] S Ishihara, T Egami, and M Tachiki. Enhancement of the electron-lattice interaction due to strong electron correlation. *Physical Review B*, 49, 1994.

[18] Hideo Aoki, Naoto Tsuji, Martin Eckstein, Marcus Kollar, Takashi Oka, and Philipp Werner. Nonequilibrium dynamical mean-field theory and its applications. *Reviews of Modern Physics*, 86, 2014.

[19] Walter Metzner and Dieter Vollhardt. Correlated lattice fermions in d=â dimensions. *Physical review letters*, 62, 1989.

[20] Walter Metzner. Linked-cluster expansion around the atomic limit of the hubbard model. *Physical Review B*, 43, 1991.

[21] Antoine Georges and Gabriel Kotliar. Hubbard model in infinite dimensions. *Physical Review B*, 45, 1992.

[22] Takeo Matsubara. A new approach to quantum-statistical mechanics. *Progress of theoretical physics*, 14, 1955.

[23] Guy Cohen, David R Reichman, Andrew J Millis, and Emanuel Gull. Green's functions from real-time bold-line monte carlo. *Physical Review B*, 89, 2014.

[24] Th Pruschke, Dan L Cox, and Mark Jarrell. Hubbard model at infinite dimensions: Thermodynamic and transport properties. *Physical Review B*, 47, 1993.

[25] JH Shim, Kristjan Haule, and Gabriel Kotliar. Modeling the localized-to-itinerant electronic transition in the heavy fermion system ceirin5. *Science*, 318, 2007.

[26] E Müller-Hartmann. Müller-hartmann, e., 1984, z. phys. b: Condens. matter 57, 281. *Z. Phys. B: Condens. Matter*, 57, 1984.

[27] Camille Aron, Gabriel Kotliar, and Cedric Weber. Dimensional crossover driven by an electric field. *Physical review letters*, 108, 2012.

[28] Naoto Tsuji, Takashi Oka, and Hideo Aoki. Nonequilibrium steady state of photoexcited correlated electrons in the presence of dissipation. *Physical review letters*, 103, 2009.

[29] Martin Eckstein and Marcus Kollar. Near-adiabatic parameter changes in correlated systems: influence of the ramp protocol on the excitation energy. *New Journal of Physics*, 12, 2010.

[30] Marin Bukov, Luca D'Alessio, and Anatoli Polkovnikov. Universal high-frequency behavior of periodically driven systems: from dynamical stabilization to floquet engineering. *Advances in Physics*, 64, 2015.

[31] Tomotaka Kuwahara, Takashi Mori, and Keiji Saito. Floquet–magnus theory and generic transient dynamics in periodically driven many-body quantum systems. *Annals of Physics*, 2016.

[32] Gaston Floquet. Sur les equations differentielles lineaires. *Ann. ENS [2]*, 12, 1883.

[33] JH Mentink, Karsten Balzer, and Martin Eckstein. Ultrafast and reversible control of the exchange interaction in mott insulators. *Nature communications*, 2015.

[34] Marin Bukov, Michael Kolodrubetz, and Anatoli Polkovnikov. Schrieffer-wolff transformation for periodically driven systems: strongly correlated systems with artificial gauge fields. *Physical review letters*, 116, 2016.

[35] Saar Rahav, Ido Gilary, and Shmuel Fishman. Effective hamiltonians for periodically driven systems. *Physical Review A*, 68, 2003.

[36] Nathan Goldman, J Dalibard, Monika Aidelsburger, and NR Cooper. Periodically driven quantum matter: The case of resonant modulations. *Physical Review A*, 91, 2015.

[37] André Eckardt and Egidijus Anisimovas. High-frequency approximation for periodically driven quantum systems from a floquet-space perspective. *New journal of physics*, 17, 2015.

[38] Naoto Tsuji, Takashi Oka, Philipp Werner, and Hideo Aoki. Dynamical band flipping in fermionic lattice systems: An ac-field-driven change of the interaction from repulsive to attractive. *Physical review letters*, 106, 2011.

[39] JM Zhang and Y Liu. Fermiâs golden rule: its derivation and breakdown by an ideal model. *European Journal of Physics*, 37(6):065406, 2016.

[40] Juan Jose Mendoza-Arenas, Fernando Javier Gómez-Ruiz, Martin Eckstein, Dieter Jaksch, and Stephen R Clark. Ultra-fast control of magnetic relaxation in a periodically driven hubbard model. *Annalen der Physik*, 529, 2017.

[41] T Tamaya, A Ishikawa, T Ogawa, and K Tanaka. Diabatic mechanisms of higher-order harmonic generation in solid-state materials under high-intensity electric fields. *Physical review letters*, 116, 2016.

[42] AF Kemper, B Moritz, JK Freericks, and TP Devereaux. Theoretical description of high-order harmonic generation in solids. *New Journal of Physics*, 15, 2013.

[43] Naoto Tsuji, Takashi Oka, and Hideo Aoki. Correlated electron systems periodically driven out of equilibrium: Floquet+ dmft formalism. *Physical Review B*, 78, 2008.

[44] Shambhu Ghimire, Anthony D DiChiara, Emily Sistrunk, Pierre Agostini, Louis F Di-Mauro, and David A Reis. Observation of high-order harmonic generation in a bulk crystal. *Nature physics*, 7, 2011.

Acknowledgements

I would like to express my deepest gratitude to my supervisor, Dr. Guy Cohen at Tel Aviv University, for enabling me to work in the field of nonequilibrium many body systems. Without his excellent guidance and profound knowledge, this work would not have been possible. I enjoyed the scientific environment and friendly atmosphere during the time I spent in his group very much.

Further, I would like to thank Prof. Dr. Alexander Lichtenstein for supervising me at the Hamburg University and giving me the right advice at the right time. My gratitude goes to all the group members, especially Yusuf Mohammed and Roberto Mozara, for the interesting discussions and suggestions they have given me during the last months.

Special thanks go to all my friends and my family for their immense support and constant encouragement not only during the last year but throughout all my studies.